Journal of Sol-Gel Science and Technology (2026)117:37
https://doi.org/10.1007/s10971-025-07063-2

ORIGINAL PAPER

Correlation between dopant-induced structural distortions and performance characteristics in Tb- and Zn-substituted Y-358 ceramics synthesized via sol–gel route

Gülnur Güdücü[1] · Özgür Öztürk[1] · Sedat Kurnaz[2] · Elif Aşikuzun Tokeşer[3] · Turgay Seydioğlu[4] · Ali Serol Ertürk[5] · Gürcan Yildirim[6] · Serap Safran[7,8]

Received: 8 August 2025 / Accepted: 9 November 2025
© The Author(s) 2026

Abstract

This study systematically investigates the structural, microstructural, electrical, and magnetic properties of $YBa_3Cu_5Cu_8O_\delta$ (Y-358) superconducting ceramics with partial substitution of trivalent terbium (Tb^{3+}) at Y^{3+} sites and divalent zinc (Zn^{2+}) at Cu^{2+} sites. The compositions $Y_{3-x}(Tb)_xBa_5Cu_8O_{18-\delta}$ and $Y_3Ba_5Cu_{8-x}(Zn)_xO_{18-\delta}$ ($0.0 \le x \le 0.15$) are synthesized via the sol–gel synthesis route and investigated using X-ray diffraction (XRD), scanning electron microscopy (SEM), electron dispersive X-ray (EDX), temperature-dependent resistivity (ρ–T), and vibrating sample magnetometer (VSM) measurements, along with theoretical modeling. It is determined that all synthesized ceramic samples exhibit high current-carrying capacity and superior superconducting performance, supported by efficient charge transport, excellent crystalline quality, and uniform composition, all of which were achieved through the sol–gel method, an effective and reliable approach for producing advanced high-performance ceramics. XRD analyses reveal that both dopants influence phase purity, crystallinity, lattice parameters, and oxygen ordering degree, with Tb impurity substitution inducing more pronounced impurity phase formation and lattice distortions. SEM and quantitative histogram analyses demonstrate that Tb enhances grain boundary disorder, grain misorientation, porosity, and microstructural problems, while Zn promotes more uniform grain growth, especially at moderate substitution levels. EDX analyses confirmed the successful substitution of Y by Tb and Cu by Zn within the Y-358 ceramic lattice, evidencing effective dopant incorporation that correlates with improved/degraded microstructural uniformity and superconducting current pathways. ρ-T experimental results show that both Tb and Zn reduce the superconducting transition temperatures (T_c) and broaden the transition width (ΔT_c), indicating increased structural disorder, perturbations of the pseudogap state, and reduced charge carrier concentration, and electronic density of states in Cu-O_2 planes. Notably, Tb doping causes a steeper decline in T_c parameters and mobile hole carrier concentration (p), attributed to its larger ionic radius and stronger lattice strain effects. Magnetic hysteresis (M–H) measurements and critical current density calculations confirm a deterioration in flux pinning capacity and superconducting performance with increased doping, particularly in the Tb-substituted Y-358 ceramics. The normalized pinning force analyses further reveal that the dominant flux pinning mechanism shifts from normal point pinning to $\Delta\kappa$-type with increasing impurity levels. Accordingly, the results demonstrate that although both dopants disrupt the Y-358 superconducting phase, Tb^{3+} impurity has a more detrimental impact on phase

✉ Gürcan Yildirim
yildirim_g@ibu.edu.tr

[1] Department of Electrical and Electronics Engineering, Kastamonu University, Kastamonu, Türkiye

[2] Central Research Laboratory, Kastamonu University, Kastamonu, Türkiye

[3] Department of Metallurgy and Materials Engineering, Kastamonu University, Kastamonu, Türkiye

[4] Department of Electronics and Automation, Kastamonu University, Kastamonu, Türkiye

[5] Department of Basic Pharmaceutical Sciences, Adiyaman University, Adiyaman, Turkey

[6] Department of Mechanical Engineering, Bolu Abant Izzet Baysal University, Bolu, Türkiye

[7] Department of Physics, Ankara University, Ankara, Türkiye

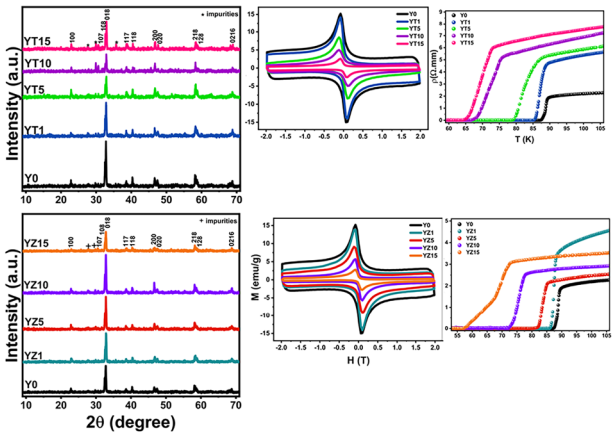
[8] Ctr Excellence Superconduct Res, 50 Year Campus, Ankara, Türkiye

Published online: 05 February 2026

stability, flux pinning, and superconducting properties due to its greater tendency to induce structural disorder. These findings underscore the critical role of dopant type and concentration in tailoring the functional properties of high-T_c Y-based superconductors for potential applications in high-temperature superconducting systems, energy devices, and magnet-based technologies.

Graphical Abstract

Comprehensive Analysis of Structural, Electrical, and Magnetic Properties in Tb^{3+}- and Zn^{2+}-Substituted Y-358 Superconducting Ceramics



Keywords Y-358 · Sol-gel · Substitution mechanism · Superconductivity, Magnetic Properties · Critical Current Density · Flux Pinning

Highlights

- Tb^{3+} and Zn^{2+} doping trigger distinct structural and superconducting responses in Y-358.
- Tb^{3+} ions cause severe lattice disruption, degrading superconducting phase integrity.
- Zn^{2+} enhances grain refinement and stability, preserving superconductivity at low levels.
- Doping alters flux pinning from point-type to $\Delta\kappa$-type, weakening vortex trapping.
- Superconducting performance is highly sensitive to dopant identity and concentration.

1 Introduction

Since the advent of high-temperature superconductors (HTSCs), YBCO compounds have been at the forefront due to their high Tc, robust grain connectivity, and technological relevance. The parent phase Y-123, with two Cu-O_2 planes and one CuO chain in an orthorhombic structure, exhibits $T_c \approx 90$–94 K, while further exploration yielded more complex phases such as Y-124, Y-247, and the recently identified Y-358 [1–6]. Structurally, Y-358 contains five Cu-O_2 planes and three CuO chains per formula unit, separated by BaO layers, which extend the c-axis lattice parameter to ~31 Å and create a richer network of conduction planes and charge reservoirs. This unique stacking is associated with enhanced anisotropy and potentially higher carrier mobility. However, the synthesis of pure Y-358 is challenging due to intrinsic structural instability and strong intergrowth with Y-123, Y-124, and secondary phases. Its sensitivity to synthesis conditions makes phase purity difficult to achieve, yet critical, as it directly dictates the superconducting performance of this complex YBCO phase [2, 6–17].

In this study, the substitution mechanism in Y-358 is examined independently of dopant valence, with emphasis placed on its structural and superconducting implications. The central aim is to elucidate how homovalent substitutions, such as Tb^{3+} for Y^{3+}or Zn^{2+} for Cu^{2+} affect crystalline quality, lattice distortions, grain boundary characteristics, magnetic behavior, and superconducting phase stability. By introducing ions of identical valence but different radii, the work investigates how local lattice distortions and electronic modifications influence superconducting pathways, pinning mechanisms, and oxygen stoichiometry. Tb^{3+} incorporation at the Y-site is expected to generate distortions that impact both superconducting and mechanical responses, while Zn^{2+} substitution at the

Cu-site may alter the electronic structure and disrupt Cu-O_2 plane coherence [18, 19]. These modifications are anticipated to regulate critical parameters such as critical temperatures, interlayer coupling, and defect tolerance in the metastable Y-358 phase relative to Y-123 superconducting phase. Ultimately, this study bridges fundamental and applied perspectives by clarifying the microstructural and electronic consequences of homovalent doping and identifying optimization strategies to enhance the superconducting and magnetic field resistance of Y-358 ceramics, synthesized via the sol-gel (SG) preparation method for future applications. Our motivation for employing the SG method in the synthesis of Y-358 ceramic superconductors arises from its well-established ability to produce high-purity, homogeneous, and stoichiometrically controlled materials at relatively low processing temperatures. Unlike conventional high-temperature solid-state or vacuum-based techniques (such as PIT, CVD, spray pyrolysis), the SG approach offers reduced energy consumption, simplified equipment requirements, and improved compositional uniformity, making it both cost-effective and environmentally favorable [20–23].

The SG route relies on the hydrolysis and polycondensation of metal alkoxides or salts, which enables uniform distribution of metal cations at the molecular scale. In practice, the process involves dissolving stoichiometric ratios of Y-, Ba-, and Cu-based nitrates or acetates in a chelating solution (commonly citric acid or ethylene glycol), followed by controlled gelation, drying, and calcination, forming a polymerized gel network upon heating at ~80–90 °C. Subsequent heat treatment at ~850–900 °C promotes crystallization and phase formation, while final sintering at 920–950 °C yields dense ceramic pellets with well-aligned grains with fine grain connectivity and controlled particle sizes (~ 200–400 nm after calcination). This molecular-level mixing method not only accelerates phase formation compared to conventional methods but also produces uniform ion distribution and facilitating enhanced reactivity during thermal treatment.

Additionally, the SG method permits straightforward incorporation of dopants and secondary phases, enabling systematic tuning of microstructure, flux pinning, and mechanical reinforcement. These advantages make SG synthesis a versatile and scalable pathway for optimizing the crystallinity, phase purity, and superconducting performance (T_c, J_c, and flux pinning capability) of Y-358 ceramics, thereby advancing their suitability for both fundamental investigations and applied superconducting technologies. The experimental results offer new scientific insights into the interplay between dopant type, microstructural evolution, and the functional properties of complex superconductors, consequently contributing to the rational design of advanced high-temperature superconducting materials with optimized performance for future technological applications.

Earlier studies on Y-358 have mainly addressed structural characterization and phase stability, reporting difficulties in synthesizing stoichiometrically pure single-phase samples due to the intrinsic instability of the compound and the strong tendency toward intergrowth with Y-123, Y-124, or secondary phases. In particular, doping strategies involving rare-earth substitutions (e.g., Tb/Y) and cationic replacements (e.g., Zn/Cu) have been explored to tune phase stability and mechanical behavior. For example, our prior work demonstrated that such substitutions influence microstructural uniformity and Vickers hardness, with the indentation-induced cracking (IIC) model providing the most accurate description of the elastic–plastic transition [18]. Similarly, investigations into Y-123 ceramics have largely focused on fluctuation-induced conductivity and particle distribution, clarifying how dopants affect carrier transport and superconducting performance [19].

However, a comprehensive structure–property correlation study for Y-358 superconducting ceramics, integrating crystallographic quality, microstructural features, charge carrier dynamics, and magnetic performance, remains largely unexplored. Most existing works are limited to either structural–mechanical aspects or isolated superconducting measurements, without systematically linking crystallography, microstructure, and transport behavior to superconducting and magnetic responses.

The present work addresses this gap by systematically investigating the electrical, superconducting, crystallographic, and microstructural properties of Y-358 superconducting ceramic structures. Special emphasis is placed on correlating charge carrier concentrations, critical current density, flux pinning mechanisms, and magnetic behavior (M–H loops, hysteresis, coercivity, and remanent magnetization) with crystal quality and microstructural features, including detailed histogram analyses and particle size distributions. This integrated approach provides new insights into the fundamental dynamics of the Y-358 phase and establishes design principles for optimizing its stability and performance in advanced superconducting applications.

2 Materials and methods

2.1 Ceramic preparation technique

In the current work, partial substitution of Tb^{3+} with Y-site and Zn^{2+} with Cu-sites in four molar percentages ($x = 0.01$, 0.05, 0.10, 0.15) is performed to obtain one of the superconducting phases of the YBCO family (Y358 superconducting phase). The substitution process was implemented using the chemical formulations Y_{3-x}(Tb)

$_xBa_2Cu_3O_{18-\delta}$ and $Y_3Ba_5Cu_{8-x}(Zn)_xO_{18-\delta}$. In this context, ($Y(CH_3CO_2)_3$), barium acetate ($Ba(CH_3CO_2)_2$), copper(II) acetate ($Cu(CH_3CO_2)_2$), and nanopowder forms of Tb and Zn are employed as precursor materials. The sol–gel synthesis route is used to determine and control the chemical composition of all samples. Anhydrous methanol (CH_3OH) served as the diluent, while glacial acetic acid (CH_3COOH) was utilized as the primary solvent. Triethanolamine (tri(2-hydroxyethyl)amine) is added as a complexing agent and pH regulator to achieve a stable and homogeneous wet solution. Following the initial pretreatment steps, the samples are converted into powder form and subsequently subjected to a calcination process at 850 °C for three cycles, each lasting 24 h, to promote the formation of nanocrystallites. The calcined powders are then sintered at 930 °C for 24 h with a controlled heating rate of 5 °C/min. Post-sintering, the samples are annealed in an oxygen atmosphere at 500 °C for 5 h and then allowed to cool gradually to room temperature in preparation for subsequent measurements. The final powders are uniaxially pressed in air at room temperature into rectangular bar-shaped pellets with dimensions of approximately $1.5 \times 0.5 \times 0.2\,cm^3$, in order to minimize porosity and improve intergranular contact. A schematic representation of the detailed preparation method and characterization techniques employed for Y-358 ceramic structures is provided in Fig. 1. The Tb-substituted Y-358 ceramic structures are labeled based on the Tb impurity substitution ratios (x = 0.0, 0.01, 0.05, 0.10, 0.15) as Y0, YT1, YT5, YT10, and YT15, respectively. Similarly, the Zn-replaced Y-358 ceramic samples are designated as Y0, YZ1, YZ5, YZ10, and YZ15, considering to their respective Zn doping levels.

2.2 Characterization methods and calculations

The XRD diffraction peaks provide critical information for calculating several fundamental structural parameters, including crystalline quality, grain orientation and alignment distributions, average crystallite size, superconducting phase purity, lattice cell parameters, and the coupling strength between adjacent conductive Cu-O_2 planes. The XRD patterns of the bulk ceramic samples (Fig. 1) are obtained on a Bruker D8 Advance model X-ray diffractometer at a scan rate of 3°/min between $2\theta = 3\text{-}90°$ using CuK_α ($\lambda = 1.541$ Å) rays. The distance between the diffraction planes is calculated using Bragg's formula. Additionally, the XRD diffractograms, particularly the peak broadening features, are employed to evaluate the influence of substitution mechanism on the average crystallite size of bulk Y-358 superconducting materials. This is carried out using the Scherrer–Warren equation of $t = 0.941\lambda/B \cos\theta_B$, based on the full width at half maximum (FWHM) values of the five most intense

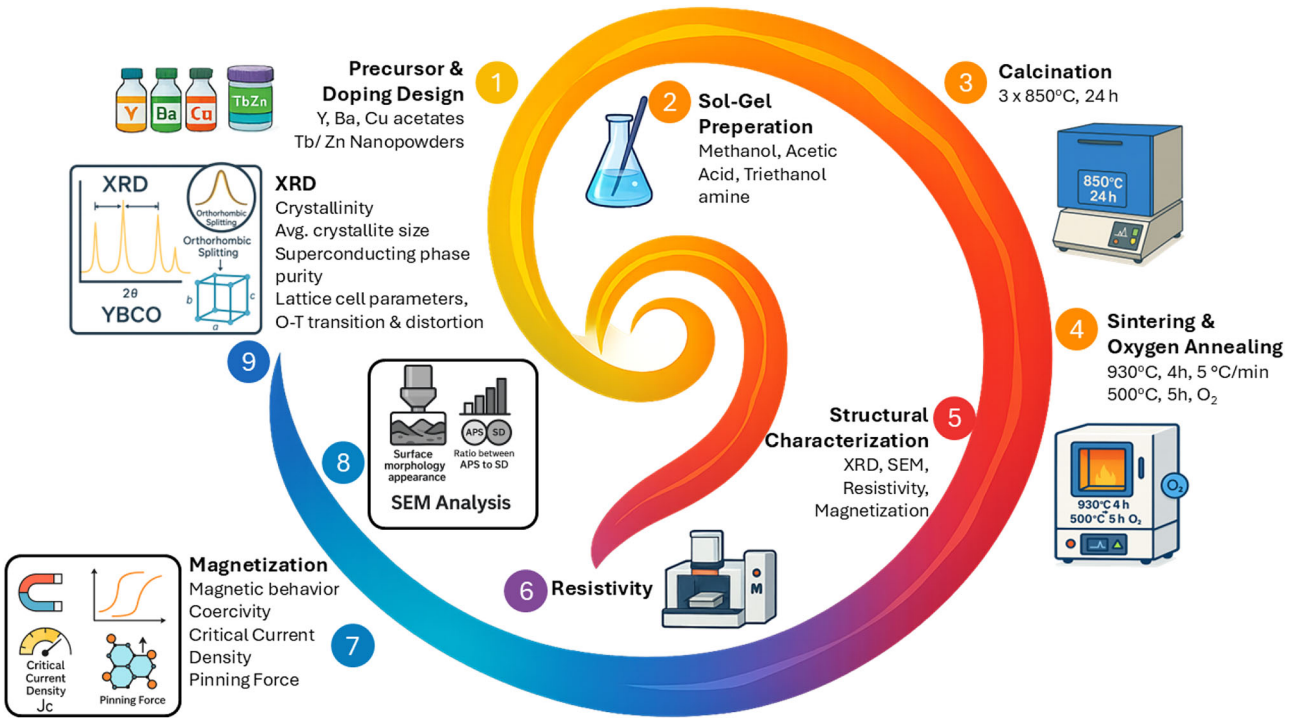


Fig. 1 A schematic representation of the detailed preparation method and characterization techniques employed for Y-358 ceramic structures is provided in Fig. 1

characteristic diffraction peaks [24, 25]. In the relation, t represents the average crystallite size, λ is the wavelength of the incident X-rays, θ_B is the Bragg angle corresponding to the diffraction peak, and B denotes the FWHM of the peak (in radians). For the calculation of lattice parameters, the bulk ceramic compounds crystallize in an orthorhombic unit cell structure with the P_{mmm} space group. The lattice constants (a, b, and c) are determined using the least-squares refinement method based on the following relation of $\frac{1}{d^2} = (\frac{h^2}{a^2} + \frac{k^2}{b^2} + \frac{l^2}{c^2})$, where d values and hkl planes show the lattice spacing and diffraction planes. Besides, the variation (based on the lattice cell constants determined within the accuracy of about ±0.01 Å) of the oxygen concentration in the Cu-O chains and Cu-O layers in the crystal system as a function of the Tb or Zn substitution level allows us to discuss the phase transition from orthorhombic to tetragonal (O-T transition) crystal structure. The orthorhombicity coefficient or orthorhombic distortion in the covalently bonded Cu–O chains is also calculated using Eq. 1 with the help of lattice parameters a and b.

$$\delta o = \frac{100(\mathrm{a} - \mathrm{b})}{(\mathrm{a} + \mathrm{b})} \tag{1}$$

The degree of orthorhombic distortion (δ_O) and the oxygen deficiency index (δ) are distinct yet interrelated quantities that describe different physical aspects of the crystal structure. The orthorhombic distortion represents a geometric measure of lattice anisotropy within the *ab*-plane arising from oxygen ordering in the Cu-O chains, whereas the oxygen deficiency index (δ) in of $YBa_3Cu_5Cu_8O_{18-\delta}$ denotes the deviation from full oxygen stoichiometry and determines the overall oxygen content and carrier concentration. Although δ_O qualitatively follows the oxygenation level, the two parameters are not quantitatively equivalent—their relationship is inverse: as δ decreases toward zero (fully oxygenated, O(1) sites filled and O(5) sites vacant), δ_O attains its maximum, corresponding to a well-defined orthorhombic structure; conversely, when δ increases (oxygen-deficient state), δ_o approaches zero, marking the transition to the tetragonal phase.

Additionally, Field Emission Scanning Electron Microscopy (FE-SEM) was performed using an FEI QUANTA FEQ 250 instrument at 10000× magnification under an accelerating voltage of 10 kV to examine the surface morphology and microstructural evolution of $Y_{3-x}(Tb)_xBa_5Cu_8O_{18-\delta}$ and $Y_3Ba_5Cu_{8-x}(Zn)_xO_{18-\delta}$ superconducting ceramics. The SEM micrographs provide detailed insights into the changes in surface texture, grain size and orientation, crystallinity quality, porosity, intergranular connectivity, and the presence of microvoids or internal defects induced by Tb/Y and Zn/Cu partial substitution mechanism. Notably, variations in particle growth and boundary coupling were analyzed to correlate dopant incorporation with microstructural coherence and densification behavior. Complementary Energy-Dispersive X-ray Spectroscopy (EDS) analyses were conducted on selected microregions to assess the homogeneity of elemental distribution and confirm the absence of foreign inclusions. The analysis confirms the effective incorporation of Tb^{3+} and Zn^{2+} ions into the Y358 crystal lattice at Y^{3+} and Cu^{2+} sites, respectively, without observable phase segregation or elemental clustering. The gradual variation in elemental intensities with increasing dopant concentration further supports homogeneous dopant diffusion and charge-compensated substitution. Combined with SEM micrographs and structural refinements, the EDX findings provide compelling evidence of successful lattice substitution and compositional uniformity, correlating well with the observed improvements in microstructural connectivity, phase purity, and superconducting performance of the modified Y358 ceramics.

At the same time, DC electrical resistivity measurements are made by a Janis CCS-450 cryostat in the temperature range of 10–300 K using the four-probe technique under a direct current of 5 mA. The contacts are made by highly conductive silver paint to prevent additional resistance. The experimental curves are used to determine the numerical values of offset/onset transition temperatures (T_c^{offset} and T_c^{onset}), and degree of broadening ($\Delta T_c = T_c^{onset} - T_c^{offset}$) parameters. The relationship between the substitution mechanism and metallic behavior is also established. At the same time, it is well established that determining the mobile hole carrier concentration p in the Cu-O_2 planes, which are primarily responsible for superconductivity in YBCO compounds, is essential for elucidating the variations in superconducting properties induced by cation substitution. Previous studies [26–32] have demonstrated that, for many HTSC systems, temperature-dependent thermoelectric power exhibits a strong correlation with the normalized transition ratio (T_c/T_c^{max}). This correlation provides a reliable approach for estimating p [26–32] and thereby offers valuable insight into the doping dependence of superconducting behavior. In the present study, the hole concentration is determined using the empirical T_c/T_c^{max} relationship, which provides a semi-quantitative estimation of carrier density in the Cu-O_2 planes [26]. This approach is widely adopted in the analysis of HTSC systems, as it directly links the superconducting transition temperature to the effective doping level.

$$p = 0,16 - \left[\left(1 - \frac{\frac{T_c^{offset}}{T_c^{max}}}{82,6}\right)\right]^{1/2} \tag{2}$$

Additionally, magnetization measurements are made using a Lakeshore 7400-S model VSM. All measurements are performed at a temperature of 20 K with an external

magnetic field of ±2 T. The M-H magnetic hysteresis (M–H) loops are used for calculating coercivity, remanent magnetization, and critical current density (maximum current that can pass in the superconducting phase) values within the grains using Bean's critical state model in Eq. 3. [33].

$$J_c(H) = 20\frac{\Delta M}{a\left(1-\frac{c}{3a}\right)} \tag{3}$$

In the equation, J_c displays the critical current density per cm when $\Delta M = M_+ - M_-$ presents the magnetization difference determined from the magnetization hysteresis loops. The flux pinning force (F_p) is an important parameter determining the pinning mechanism of fluxoids in the crystal system. For extended analysis of pinning type, three theoretical models relying on (i) the geometry of defects (point, linear, planar, or surface), (ii) the type of interaction (core or magnetic), and (iii) the type of pinning centers (normal or superconductor) were used. The pinning force values of the samples were interpreted by comparing them with the three theoretical models given in Eqs. 4–6 [34].

$$\Delta\kappa\text{pinning} : \mathrm{f_p(b)} = 3\mathrm{b}^2(1-2\mathrm{b}/3) \tag{4}$$

$$\text{Normal point pinning} = f_p(b) = 9/4b(1-b/3)^2 \tag{5}$$

$$\text{Normal surface pinning} = f_p(b) = 25/16b^{\frac{1}{2}}\left(1-\frac{b}{5}\right)^2 \tag{6}$$

where, $b=H/H_{\max}$, $f_p\ (b)=F_p/F_{max}$. The results derived from the applied theoretical models enabled detailed interpretations regarding the presence of secondary impurity phases, oxygen deficiencies within the crystal lattice, and weakly bonded grain boundaries in newly synthesized Y-358 superconducting samples.

3 Results and discussion

3.1 XRD results

The effects of partial substitution of trivalent Tb ions at the Y-sites and, separately, divalent Zn ions at the Cu-sites on the crystallization behavior, crystallinity quality, phase volume fractions, average crystallite size, lattice parameters, orthorhombic-to-tetragonal phase transition, orthorhombicity, and oxygen concentration within the covalently bonded Cu-O chains of the Y-358 superconducting phase are systematically investigated through powder XRD analysis. The structural modifications are examined by analyzing the characteristic reflection peaks observed in the XRD diffractograms. The diffraction patterns corresponding to all superconducting ceramic structures are presented in Fig. 1. The calculated structural parameters for both Tb- and Zn-replaced Y-358 superconductors are numerically depicted in Table 1.

Table 1 Crystallite size, lattice cell parameters, unit cell volume, and orthorhombicity coefficient for Tb- and Zn-substituted Y-358 samples

Sample	Crystallite size (nm)	a(Å)	b(Å)	c(Å)	V(Å^3)	δ
Y0	28.4 ± 0.6	3.894	3.831	31.445	469.103	0.812
YT1	30.0 ± 0.5	3.894	3.820	31.663	470.953	0.961
YT5	26.1 ± 0.5	3.887	3.824	31.688	471.036	0.809
YT10	25.7 ± 0.6	3.887	3.815	31.528	467.531	0.928
YT15	25.4 ± 0.6	3.889	3.820	31.054	461.337	0.900
YZ1	29.9 ± 0.6	3.880	3.822	31.615	468.814	0.749
YZ5	29.0 ± 0.4	3.889	3.824	31.662	470.941	0.840
YZ10	28.1 ± 0.6	3.894	3.827	31.409	468.010	0.872
YZ15	27.9 ± 0.5	3.892	3.829	30.899	460.412	0.812

For Tb-doped Y-358 samples, the XRD patterns (Fig. 2a) show that the substitution of Y^{3+} (90 pm) ions with larger Tb^{3+} (92 pm) ions leads to the formation of some impurity phases. However, the orthorhombic structure of the Y-358 phase is still maintained, even at the highest doping levels. These findings indicate that the successful synthesis of ceramic materials exhibiting the desired crystalline quality underscores the significance of the SG method as an effective and reliable technique for the preparation of high-performance ceramic systems.

With increasing Tb impurity content, the intensity of the main diffraction peaks is reduced, and additional impurity peaks become more visible, especially for x ≥ 0.05. These impurity peaks, marked with asterisks (*) and plus signs (+), are likely related to $BaCuO_2$ and $BaTbO_3$ phases, and a peak to the right of the main (018) peak may be attributed to $BaCO_3$ [35, 36]. It is found that the Y-358 superconducting phase is more sensitive to Tb impurity substitution and more prone to impurity formation compared to the more stable Y-123 phase [18, 19]. Lattice parameter analysis (Table 1) reveals that the *a* and *b* parameters show almost no significant change with increasing Tb concentration, while the *c* parameter initially increases up to 0.05 Tb impurity content and then decreases at higher concentrations, indicating no clear systematic trend. At lower Tb ion concentrations (0.01 and 0.05), crystallite size increases slightly from 28.35 nm to 29.98 nm (for YT1), indicating an initial promotion of grain growth; however, at higher Tb concentrations (0.10 and 0.15), crystallite size decreases towards 25.43 nm for the YT15 ceramic structure, indicating that excessive Tb content adversely affects grain growth and crystallinity due to the disrupted crystal order and weakened interatomic interactions. Additionally, the

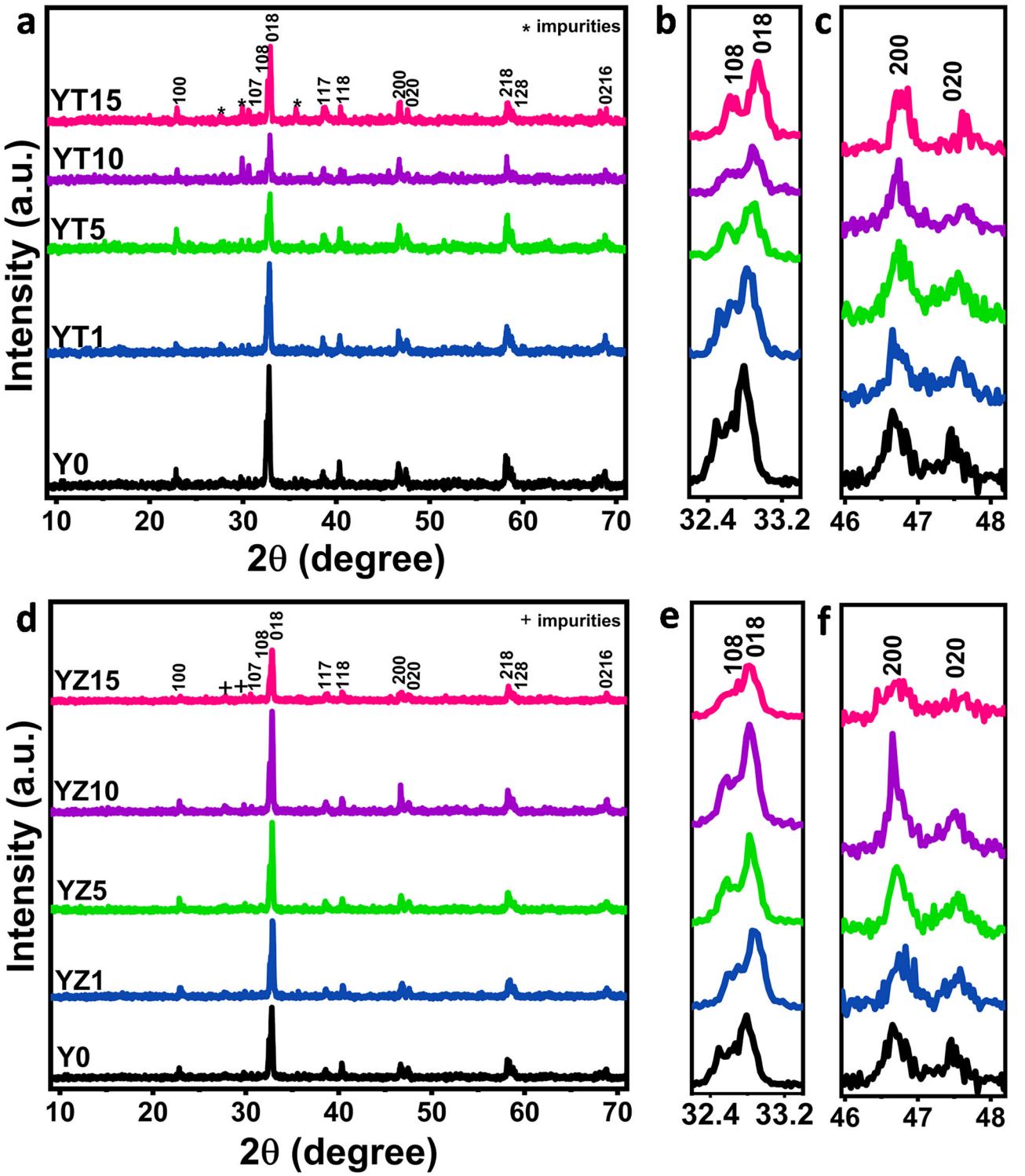


Fig. 2 XRD patterns of **a**) Tb-doped Y-358 samples and expanded views of **b**) (108)-(018) peaks and **c**) (200)-(020) peaks; **d**) Zn-doped Y-358 samples and expanded views of **e**) (108)-(018) peaks and **f**) (200)-(020) peaks. Peaks marked with asterisks (*) and plus signs (+) indicate impurity phases [19]

main peaks [(108)-(018) and (200)-(020)] shift slightly toward higher angles as the substitution level increases, which reveals lattice contraction and increased lattice strain in the crystal lattice (Fig. 2b, c). The separation of (108)-(018) and (200)-(020) peaks, together with the higher intensity of (108) and (200) compared to (018) and (020), confirms the formation of the orthorhombic superconducting phase.

For Zn-substituted Y358 ceramic structures (Fig. 2d), XRD patterns show that Zn^{2+} (74 pm) ions, expected to substitute at Cu^{2+} (73 pm) sites, do not introduce any new sharp impurity peaks. The orthorhombic structure is well preserved across all replacement levels. Only a few weak impurity peaks are visible, mostly at higher Zn contents ($x = 0.10$ and 0.15), indicating that Zn ions are better integrated into the lattice compared to Tb particles. The calculated lattice parameters in Table 1 for Zn-substituted ceramic structures indicate negligible variation in a and b lattice cell parameters, while the c-axis length exhibits no systematic trend, with a distinct decrease observed only at the highest Zn concentration ($x = 0.15$). The crystallite size increases slightly from 28.35 nm to 29.89 nm up to 5% Zn, then decreases for higher replacement ratios, which may be related to the easier incorporation of Zn ions into the structure up to a certain limit. In this respect, the smallest crystallite size of 27.91 belongs to the YZ15 sample. The similar results can be observed for the other RE-358 ceramic structures. Namely, the refined lattice parameters obtained from Rietveld analysis for the Sm-358 and Gd-358 phases are summarized as follows. For Sm-358, the lattice constants were determined to be $a = 3.868(3)$ Å, $b = 3.889(8)$ Å, and $c = 31.183(1)$ Å, with an average crystallite size of 59.3 ± 19.7 nm. In comparison, the Gd-358 phase exhibited slightly smaller lattice parameters of $a = 3.852(0)$ Å, $b = 3.883(0)$ Å, and $c = 31.120(0)$ Å, accompanied by a crystallite size of 60.1 ± 22.3 nm [37].

When comparing all substitution ratios for both Tb and Zn foreign impurities in Y-358 ceramic superconducting samples in the current work, it is clear that impurity formation and reduction in diffraction peak intensity are more pronounced in Tb-replaced samples than in Zn-doped ones. The main diffraction peaks in Zn-substituted ceramics are generally sharper and better separated, and the 10% Zn-doped sample especially shows the highest orthorhombicity and the best crystallinity. However, at 15% doping for both Tb and Zn, there is a clear decrease in crystallinity, a reduction in the separation of the main peaks, and lower unit cell volumes, all of which indicate higher structural disorders, grain misorientation, impurity scatterings, porosity, and grain boundary problems. In more detail, both Tb and Zn substitutions are found to modify δ_O through lattice strain and oxygen redistribution within the Cu-O chain network. For Tb-doped ceramics, the introduction of larger Tb^{3+} ions (92 pm) in place of Y^{3+} (90 pm) induces enhanced lattice distortion, peak broadening, and impurity formation, while preserving the orthorhombic framework up to moderate doping levels. Zn^{2+} substitution, by contrast, produces smaller lattice perturbations and maintains better phase stability. The degree of orthorhombicity decreases with increasing dopant content in both series, indicating partial oxygen loss and structural disorder. These changes are consistent with reduced carrier concentration and weakened interlayer coupling, which collectively govern the observed degradation in superconducting transition temperature and current density. As shown in Table 1, the YT5 and YZ1 compositions exhibit the lowest δ_O values of 0.809 and 0.749, respectively, highlighting the significant impact of the substitution mechanism on the oxygen sublattice and its subsequent influence on superconductivity.

In Zn-doped samples, only one or two small impurity peaks with low intensity are also observed, usually between 26° and 30°, while Tb-doped samples show more obvious impurity peaks at these angles, particularly at 10% and 15% substitution levels. These extra peaks are likely related to secondary phases such as Y-211, $BaCuO_2$, $BaTbO_3$, and $BaCO_3$, and sometimes a peak near 36° becomes more pronounced as the substitution amount increases. This indicates that the substitution of Tb and Zn foreign impurity ions becomes more difficult at high levels, leading to the growth of more impurity phases and possibly even the formation of the Y-123 superconducting phase as a secondary phase. This is because the Y-358 superconducting phase is less stable than other YBCO phases, especially at high dopant concentrations. It is sometimes hard to distinguish Y-358 from other phases like Y-123 and Y-112 just by examining at the XRD patterns. Consequently, although both Tb and Zn ions introduce structural distortions and impurity-related disruptions within the Y-358 superconducting phase, the adverse effects induced by Tb ions are more pronounced. This is primarily attributed to the larger ionic radius of Tb^{3+} particles, which leads to greater lattice strain and instability, whereas Zn^{2+} ions integrate more compatibly into the crystal lattice, causing comparatively less structural perturbation.

3.2 SEM investigations

3.2.1 Surface morphology appearance for Y-358 ceramic matrices

Figure 3 shows the SEM images of the un-substituted, Tb-substituted, and Zn-substituted Y-358 bulk ceramic samples. The microstructure of the Y0 displays a mixture of rod-like and round grains, with some grape-like clusters forming along the grain boundaries. The surface is not fully flat, and there are some porous regions, pointing out that the crystal formation is not completely homogeneous [19]. However, due to the inherent non-flatness of the sample surfaces, the pixel intensity values obtained from secondary electron imaging (SEI) may be influenced by surface roughness. Such effects can result in apparent distortions or broadened distributions in high-magnification images, as increased curvature enhances electron scattering and image contrast. Nevertheless, the complementary results obtained

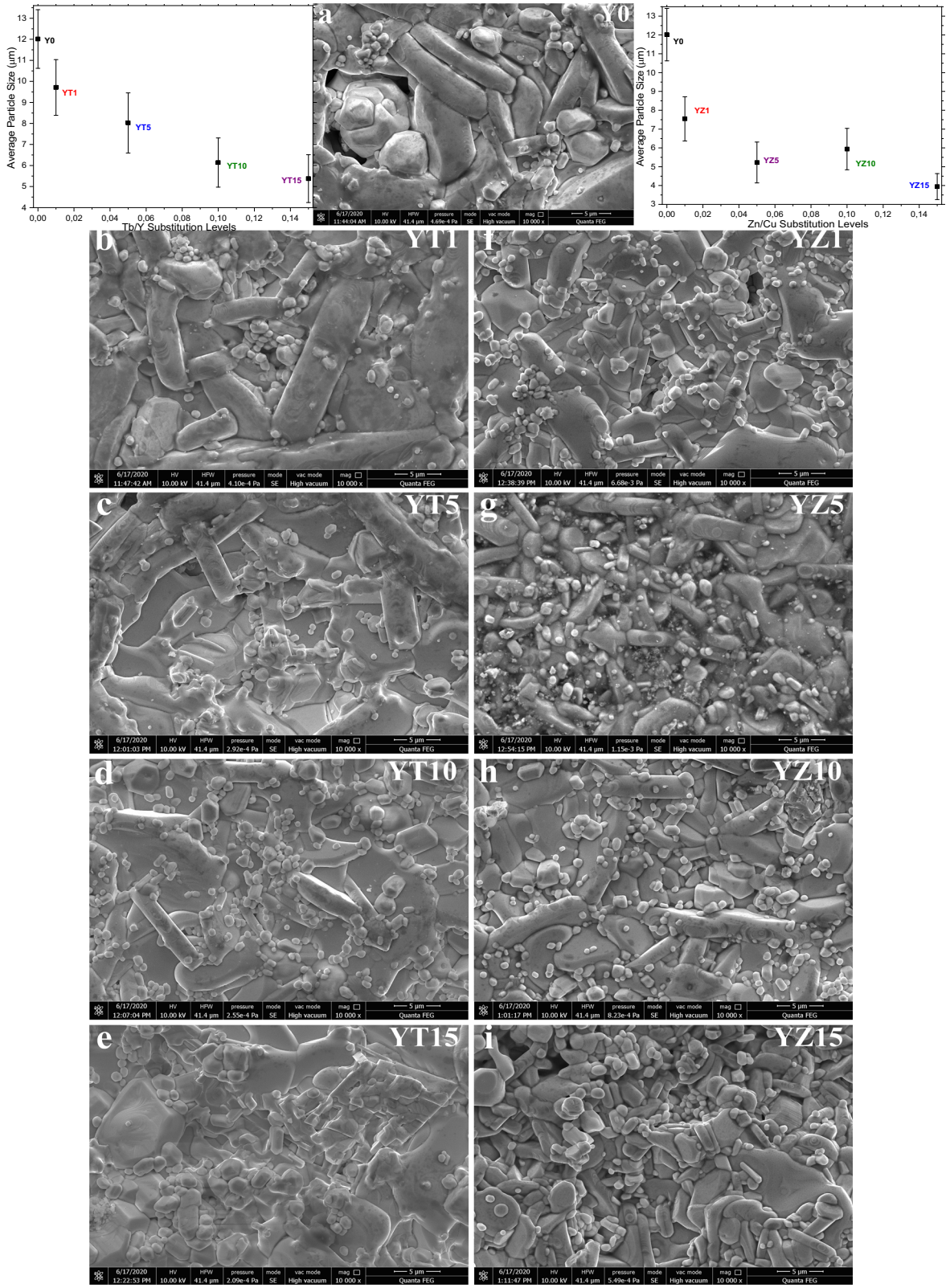


Fig. 3 SEM images of **a**) Y0, **b**) YT1, **c**) YT5, **d**) YT10, **e**-) YT15, **f**) YZ1, **g**) YZ5, h-) YZ10, and **i**) YZ15 samples. Left- APS parameters for Tb-substituted ceramic structures and Right- Zn-substituted structures

from average particle size analysis and electrical-superconducting measurements corroborate the SEM observations, thereby reinforcing the validity of the interpretations presented in this study.

When low levels of Tb are added, the grain size becomes smaller and the grains are more evenly distributed. The SEM images show that Tb doping encourages the formation of smaller grains and increases the number of nucleation sites, likely due to the larger size of Tb^{3+} ions compared to Y^{3+}. As the Tb doping increases to 10%, the grains are more densely packed, and the boundaries between grains become less clear. However, at the highest doping, the grains turn irregular and less uniform. There is also more porosity, and the grains start to form clusters. This shows that too much Tb forms defects, which can negatively affect the microstructure. Thus, while moderate Tb doping can help to refine grains and improve properties, excessive Tb can cause larger intergranular stress accumulations, melt particle coalescence, bond weakening, microstructural flaws/disorders, and porosity based on the lattice instability and reduced crystallization temperature. The degradations in the microstructural quality, uniform particle growth, and interlayer connections correlate with the experimentally observed declines in crystallographic integrity, crystal quality, surface morphology appearance, structural stability, and magnetization performance quantities of Y-358 ceramic structures.

The Zn-substituted samples show different trends. According to Fig. 3, in the bulk YZ1 ceramic compound, the particles are smaller than in the undoped sample, and there is more porosity. When Zn is increased to 5%, the grains look more irregular and less connected, and there are more pores and microcracks. At YZ10 ceramic structure, the grains actually appear a bit larger and more regular again, and the latter sample possesses fewer pores and cracks compared to the YZ5 sample. As for YZ15 sample, the structure is breaking down again, supported by average particle size analysis. This change may be because Zn reaches its solubility limit in the structure, which can act as a flux to help grain growth. This is also supported by a previous publication [19]. Furthermore, the presence of different ions in the crystal system exhibits various effects on surface morphology of the YBCO ceramic structures. For example, in the literature, the RE-358 superconductors exhibit homogeneously distributed micrometric grains with compact, low-porosity surfaces and well-defined boundaries, indicating limited intergranular diffusion, particularly in the Gd-358 phase [37]. In contrast, the Sm-358 phase shows finer grains that agglomerate locally, inducing slight lattice disorder that enhances vortex pinning and transport performance. No impurity phases were detected, confirming phase purity, while sintering promoted strong grain adhesion and fine-grained densification [9, 37, 38]. The similar granular morphology is observed for the Eu, Dy, and Ho substituted YBCO ceramic superconductor systems [10, 39, 40].

In the current work, comparing all SEM results shows that both Tb and Zn substitutions affect the surface morphology appearance, microstructural quality, uniform particle growth, interlayer connections, and porosity of Y-358 superconductors, but in different ways. Increasing Tb ion contents cause the grain structure to become more disordered and porous, with wider, more irregular grain boundaries and the appearance of cluster-like accumulations. At high levels of Tb, the structure becomes especially porous and less uniform. For Zn doping, the grain boundaries also become more irregular, and the porosity increases at low and moderate Zn levels, but at the 10% Zn concentration, grain uniformity improves and porosity decreases somewhat. At the highest Zn substitution level, a noticeable reduction in particle size, consistent with the supporting evidence from other characterization results. All the findings and interpretations reveal that although both dopants introduce microstructural disruptions, terbium ions exhibit a greater tendency to enhance porosity and structural disorder, whereas zinc particles, particularly at 10% Zn concentration, can contribute to grain growth and improved microstructural connectivity. This is clearly demonstrated by evaluating the average particle size of the un-substituted, Tb-substituted, and Zn-substituted Y-358 bulk ceramic samples.

3.2.2 Detailed histogram analyses of ceramic structures

Histograms serve as valuable tools for quantitatively evaluating differences in porosity, surface morphology, surface texture, and grain connectivity by representing the frequency distribution of pixel intensity values (frequency distribution of grain sizes estimated from SEM micrographs) across a grayscale image. The x-axis of a histogram corresponds to pixel brightness levels, ranging from 0 (pure black) to 255 (pure white), while the y-axis denotes the number of pixels at each intensity level. In the context of this study, Fig. 4a–i include both SEM micrographs and their corresponding histograms for Tb/Y and Zn/Cu substituted Y-358 ceramic superconductors. Furthermore, the slight variations observed in the histogram analyses between the Tb- and Zn-doped samples may be attributed to the distinct ionic radii and substitutional preferences of these dopants at the Y and Cu lattice sites, respectively. Scientifically sound and formal interpretation of histogram data according to surface morphology is as follows. The corresponding histograms display that the undoped Tb-free sample displays a relatively narrow and symmetric distribution, and a right-skewed intensity distribution with a dominant presence of mid-to-high pixel brightness values.

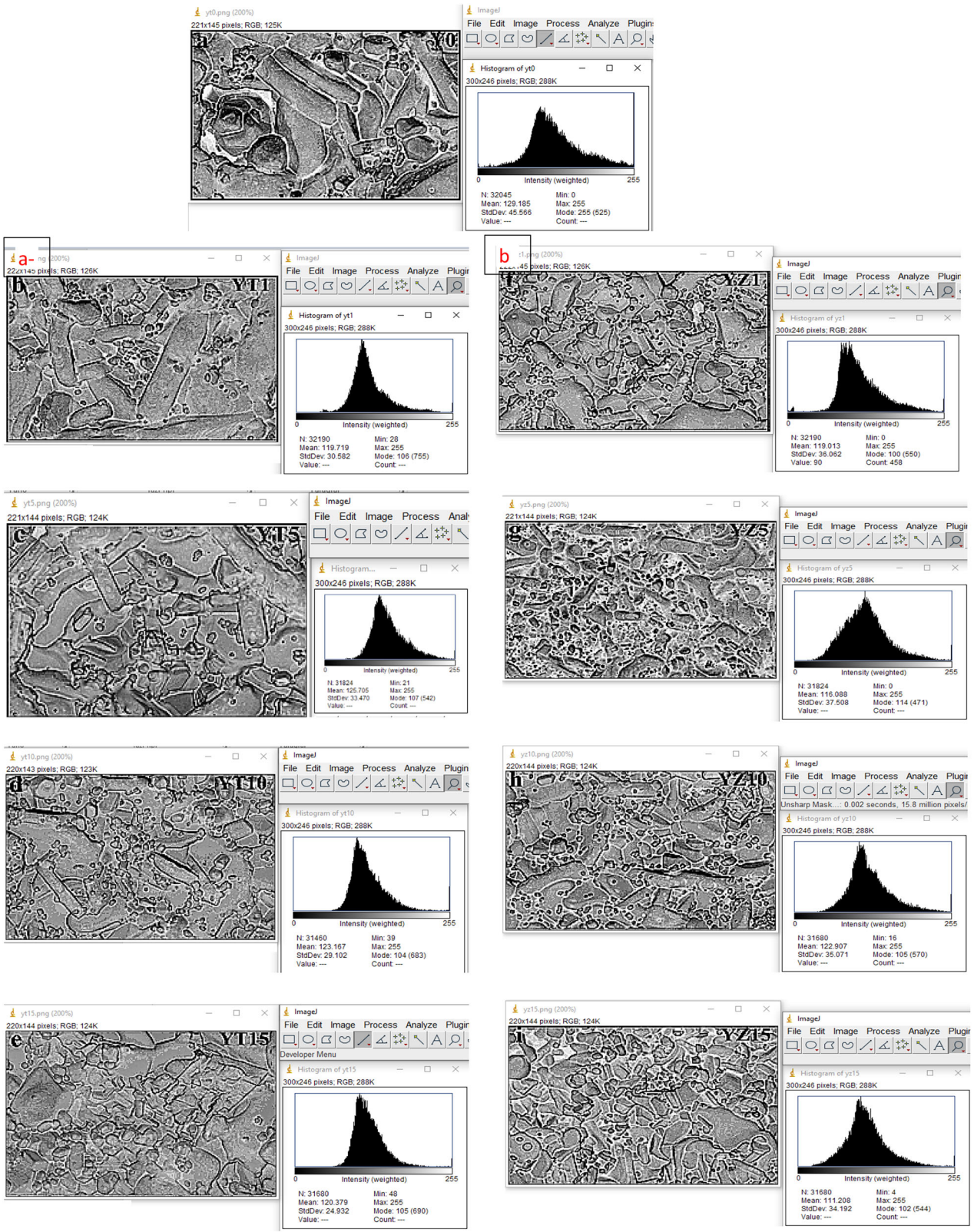


Fig. 4 Histograms for **a**) Tb-substituted and **b**) Zn-substituted Y-358 ceramic compounds

This distribution reflects a moderately dense, uniform, and compact microstructure (with balanced proportions of bright and dark regions), consistent with the presence of rod-like and round grains and a partially porous but continuous grain network. With the progressive incorporation of Tb ions (from YT1 to YT15) in the Y-358 ceramic matrices, the histogram profile undergoes a gradual shift toward lower intensity values, broadening in distribution, and an increase in standard deviation. Namely, increasing Tb substitution (especially for YT10 and YT15) tends to degrade the microstructural homogeneity, leading to more porous and disordered surfaces, as evidenced by broader and gradually left-skewed toward lower intensity in the histogram curves. In more detail, the variations observed in the histogram profiles can be attributed to several microstructural phenomena induced by the doping level. In particular, the increased prevalence of darker pixel regions corresponds to higher porosity levels and a greater density of microcracks within the ceramic matrix. This shift in brightness distribution is primarily associated with deteriorated grain connectivity and enhanced surface irregularities, which exhibit limited lattice compatibility and hinder uniform grain development. Additionally, the emergence of larger voids and phase-separated domains further contributes to diminished surface brightness, reflecting a decline in the fundamental characteristic properties. These features collectively manifest as broader and more left-skewed histograms, indicating increased heterogeneity and degradation in the microstructural quality.

Moreover, the Zn/Cu substituted samples show a distinct trend compared to the Tb superconducting series. Zn substitution demonstrates a dual effect. Namely, while moderate Zn levels seem to support grain growth and reduce microvoids, excessive substitution begins to reverse these benefits due to possible lattice distortion. In more detail, similar to the pure superconducting sample in the series, the YZ1 sample retains a moderate and symmetric histogram, indicating a comparatively smooth and homogeneous surface. Minute Zn impurity levels (YZ1 and especially YZ5 sample), the histograms are slightly broadened with a mild shift toward darker intensities, indicating enhanced porosity, smaller grain sizes, and microcrack formation. Besides, there appears a progressive narrowing of the grayscale distribution with a mild skew toward higher intensity values, particularly evident in the YZ10 sample, confirming improved surface brightness and a potential reduction in porosity. This trend corresponds to the observed microstructural features, where higher Zn content promotes grain coarsening and the development of more well-defined, larger grains, as reflected by the sharper and more pronounced histogram peaks. The features mentioned imply enhanced grain connectivity and reduced surface roughness in localized regions. Nevertheless, the YZ15 sample still exhibits a degree of histogram broadening, slight re-sharpening, and an increase in higher-intensity pixel frequencies, indicative of residual microstructural heterogeneities. This persistent distribution width indicates that excessive Zn/Cu partial substitution likely surpasses the solubility limit of the host lattice, resulting in lattice destabilization. These microstructural disruptions compromise basic uniformity and structural coherence, despite the localized grain refinement observed at moderate doping levels. This interpretation is corroborated by SEM investigations, which reveal weakened grain connectivity, increased porosity, and the emergence of voids, all indicative of compromised microstructural integrity at higher Zn concentrations.

In summary, the histogram analyses align well with SEM-based microstructural assessments, confirming that Tb doping enhances porosity and disorder with increasing concentration, while Zn doping initially disrupts grain structure but later facilitates recrystallization and densification at relatively higher levels. The digital image analyses serve as effective, non-destructive tools to quantitatively assess the impact of different dopants on surface morphology, grain connectivity, and fundamental structural homogeneity in Y-358 superconducting ceramics.

3.2.3 Average particle sizes in Tb/Y and Zn/Cu-substituted Y-358 ceramics

The influence of substitution on the average particle size (APS) of Y-358 ceramics was investigated through SEM imaging, with quantitative analysis performed using the ImageJ software program. The analysis reveals that incorporating impurity ions significantly alters the APS values, which are measured from particles forming within characteristic rod-like and round grains, and grape-like cluster morphologies, as illustrated in Fig. 3. The corresponding APS results for all samples, is presented in left and right sides of Fig. 3. According to the APS values, while the average particle size is highest in the dopant-free sample (Y0), it shows a linear decreasing trend as the Tb content increases (Left side of Fig. 3). The decrement reduction can be attributed to the limited compatibility of Tb ions with the Y site in the crystal lattice. At higher substitution levels, Tb tends to increase the number of nucleation centers, thereby promoting the formation of a larger quantity of smaller grains. A similar trend of particle size reduction is observed with Zn substitution; however, this decrease occurs more consistently and is accompanied by a steady decline in standard deviation (SD) values. This behavior displays that Zn doping promotes a more controlled grain refinement process and leads to a more homogeneous particle distribution across the microstructure (Right side of Fig. 3). Accordingly, the average particle size exhibits a clear

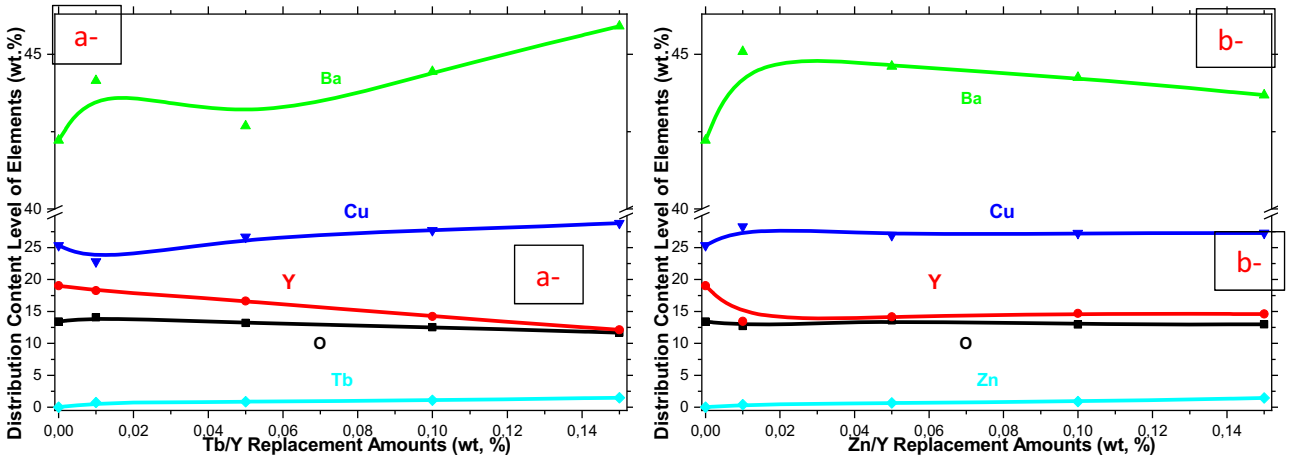


Fig. 5 Variation of experimental distribution contents (wt.%) for **a**- Tb-substituted and **b**- Zn-substituted Y-358 ceramics

decreasing trend in the following order: YO > YT1 > YZ1 > YT5 > YZ5 > YT10 > YZ10 > YT15 > YZ15, as provided in left and right sides of Fig. 3. This progression indicates that both Tb and Zn substitutions effectively reduce the particle size, with Zn-doped samples generally showing finer grain structures at comparable doping levels. As for the standard deviation values, the lower parameters obtained for all the samples (particularly in Zn-substituted samples) confirm higher measurement reliability and improved surface uniformity. In more detail, although the standard deviation values remain relatively stable across the substitution range, slight fluctuations may indicate increasing microstructural irregularities. These variations verify that excess Tb incorporation leads to blurred grain boundaries and reduced surface homogeneity, which reflect a gradual degradation in structural order. The findings are supported by the XRD findings and SEM images. Moreover, the enhanced consistency in Zn-containing samples points to a more homogeneous microstructural distribution, reinforcing the notion that Zn incorporation contributes to more uniform grain refinement and better-controlled crystal growth across the ceramic matrix.

Numerically, the APS and corresponding SD values for Tb- and Zn-substituted Y-358 ceramics are quantitatively assessed to evaluate the uniformity of particle distribution. For the Tb-substituted series, the APS values gradually decrease from 12.01 µm (Y0) to 5.38 µm (YT15), while the SD parameters remain relatively consistent, ranging between 1.14–1.43 µm (as seen in Fig. 5). In contrast, Zn-substituted samples show a similar decreasing trend in APS values, from 12.01 µm (Y0) to 3.95 µm (YZ15), accompanied by a notable reduction in SD from 1.39 µm to 0.69 µm. Correspondingly, among all samples, YZ15 exhibits the smallest APS and the lowest variance, which may indicate a well-oriented, smoother, and denser surface morphology. These characteristics imply improved microstructural uniformity and more compact grain packing at higher Zn concentrations.

We also determine the ratio of APS to SD, which is a powerful indicator of measurement reliability and is very meaningful in both materials science and broader scientific analysis. This is directly related to statistical confidence and signal-to-noise in data analysis. A higher ratio supports stronger conclusions about trends, effects of doping, or structural differences. On this basis, the ratio declines from 8.65 (Y0) to 4.73 (YT15), indicating a loss of uniform grain distribution at higher Tb levels. Besides, the APS/SD ratio for Zn-doped ceramics improves from 8.65 (Y0) to 5.75 (YZ15), indicating enhanced particle size homogeneity, especially at higher Zn concentrations. These results highlight that while both dopants reduce particle size, Zn substitution contributes more effectively to microstructural uniformity than Tb, particularly at elevated doping levels.

To sum up, the surface morphology appearance and related sections indicate that while both Tb and Zn doping affect grain morphology and connectivity between the superconducting stacked layers, Zn appears to exert a more stabilizing influence on microstructure, particularly at higher substitution levels, likely due to its solubility and role in promoting phase homogeneity. In contrast, Tb induces higher porosity and surface roughness beyond a critical concentration, limiting its microstructural benefits. These findings collectively demonstrate that dopant type and concentration play pivotal roles in tailoring the grain structure, phase distribution, structural stability, and crystallographic integrity of Y-358 ceramics.

3.3 EDX investigations

Energy-dispersive X-ray (EDX) spectroscopy was employed to quantitatively evaluate the compositional

Table 2 EDX data for local elemental composition distribution content (wt.%) for the samples

Name	Weight %				
	O_K	Y_L	Ba_L	Cu_K	Tb_K
Y0	13.43	19.02	42.22	25.33	-
YT1	14.06	18.25	44.15	22.81	0.73
YT5	13.18	16.63	42.68	26.66	0.86
YT10	12.55	14.22	44.44	27.71	1.08
YT15	11.67	12.13	45.91	28.82	1.47
	Weight %				
	O_K	Y_L	Ba_L	Cu_K	Zn_K
YZ1	12.73	13.46	45.09	28.30	0.42
YZ5	13.61	14.17	44.61	26.94	0.68
YZ10	12.94	14.68	44.25	27.25	0.88
YZ15	12.99	14.59	43.68	27.28	1.46

evolution of $Y_{3-x}(Tb)_xBa_5Cu_8O_{18-\delta}$ and $Y_3Ba_5Cu_{8-x}(Zn)_xO_{18-\delta}$ ceramics. The obtained distribution profiles of Y, Ba, Cu, O, Tb, and Zn are presented in Fig. 5. The analysis confirms that both Tb and Zn ions are successfully incorporated into the Y358 crystal matrix, substituting at Y and Cu lattice sites, respectively. The elemental concentrations determined from EDX are also summarized in Table 2.

As shown in Fig. 5a, gradual substitution of Tb^{3+} for Y^{3+} induces measurable compositional changes within the Y358 phase. Ba and Cu concentrations increase progressively with Tb incorporation, whereas Y content decreases proportionally, confirming the charge-compensated substitution mechanism. The oxygen content displays minor fluctuations, reflecting local lattice adjustments induced by Tb substitution. The monotonic rise in Tb signal intensity with increasing x further verifies effective dopant diffusion and uniform distribution across the ceramic grains.

A similar compositional trend was observed for the Zn-doped series (Fig. 5b). With increasing Zn concentration, the Cu content tends to decrease correspondingly, consistent with Zn^{2+} ions preferentially substituting Cu^{2+} sites in the Y358 crystal lattice. Ba (initially increase) and Y (initially decrease) levels remain relatively stable, indicating that the substitution process is localized within the Cu-O network. Oxygen content shows slight variation at low Zn levels but remains nearly constant at higher dopant concentrations, implying minimal impact on oxygen stoichiometry.

Consequently, EDX data reveal that both Tb and Zn dopants are incorporated in increasing amounts within the ceramic matrix and are distributed homogeneously, confirming the successful formation of solid solutions without detectable secondary phase separation. The compositional changes measured directly affect the electronic balance and microstructural evolution of the Y358 ceramic system, as observed in subsequent structural and superconducting characterizations.

3.4 DC electrical experiments

3.4.1 Superconducting parameters

Electrical resistivities as a function of environment temperatures provide critical insight into the superconducting transition and the crystal structure quality in newly synthesized Y-358 superconducting samples. The experimental measurements are especially sensitive to changes brought about by dopant type and partial substitution concentrations. Doping can trigger several mechanisms that influence resistivity, including changes in the skeleton structure, oxygen ordering, bond distances within Cu-O and Cu-O_2 planes, and the introduction of lattice strain or impurity scattering. The presence of dopant atoms affects not only the normal-state resistivity but also the T_c, ΔT_c, and the density of mobile charge carriers. Moreover, the electrical resistivity plots can reveal how doping influences metallic characteristics, superconducting transition sharpness, and the extent of disorder within the samples. Thus, factors such as porosity, grain boundary effects, and the homogeneity of oxidation states play a role in shaping the observed resistivity behavior [41–44].

Figure 6a shows the ρ-T measurements for the Tb-doped Y-358 samples. All samples with Tb doping exhibit superconducting transitions, indicating that superconductivity is preserved; however, this observation alone does not necessarily confirm the full retention of the orthorhombic structure, as percolative effects through minor orthorhombic domains could also account for the observed transitions. The transition to the tetragonal phase, by contrast, is associated with a rapid suppression of critical transition temperature. Similarly, the results obtained from XRD confirm this structural tendency. Correspondingly, the materials exhibit the intended crystalline quality and uniform compositional homogeneity.

However, as the Tb doping level increases, the T_c value decreases gradually. The decrement trend is especially strong after the doping amount exceeds 5%. The numeric values are depicted in Table 3. It is visible from the table that the Y0 has the highest superconducting transition temperatures, with T_c^{onset} at 90.01 K and T_c^{offset} at 87.13 K, as well as the lowest resistivity at room temperature and the narrowest transition width ($\Delta T_c = 2.88$ K). As the Tb impurity content increases, the transition width becomes larger, reaching 11.51 K for the highest Tb doping. Correspondingly, the presence and increasing concentration of Tb impurities may affect adversely the stabilization of superconducting clusters, disrupt the crystal quality and homogeneity of oxidation states, and hinder the delocalization of

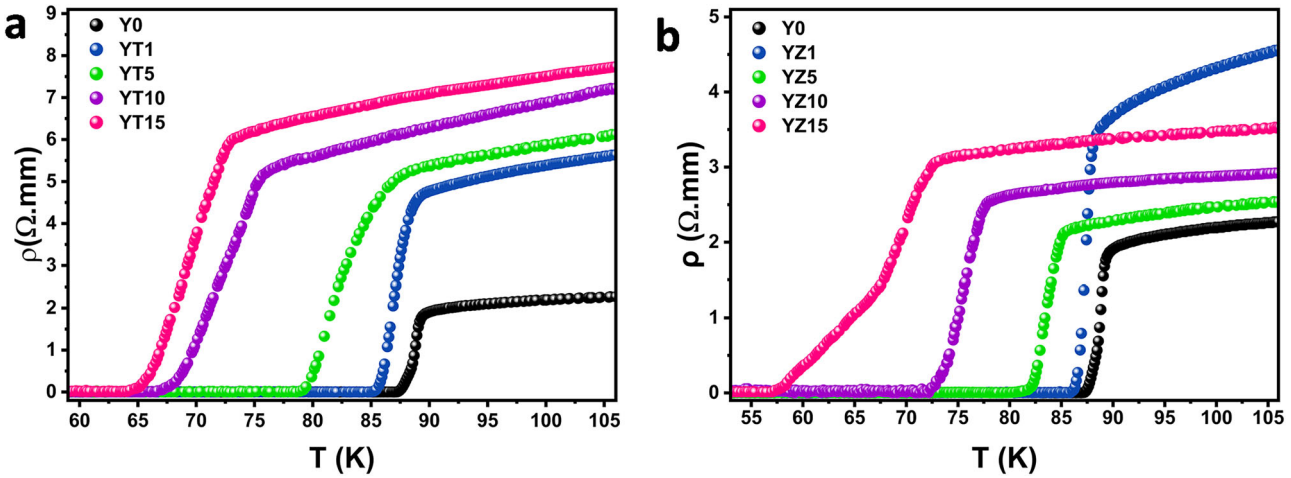


Fig. 6 Temperature dependence of electrical resistivity measurements for **a**) Tb-doped and **b**) Zn-doped Y358 samples

Table 3 Superconducting transition temperatures, transition width, and carrier concentration for Tb and Zn-doped Y358 samples from ρ–T measurements

Sample	T_c^{onset}(K)	T_c^{offset}(K)	ΔT_c (K)	p
Y0	90.01	87.13	2.88	0.118
YT1	89.90	86.21	3.69	0.117
YT5	88.27	79.15	9.12	0.108
YT10	76.91	67.13	9.78	0.096
YT15	74.74	63.23	11.51	0.092
YZ1	89.68	84.99	4.69	0.1150
YZ5	85.57	80.63	4.94	0.1096
YZ10	78.97	71.87	7.10	0.1002
YZ15	73.88	56.98	16.90	0.0869

electronic density of states. Additionally, Tb incorporation diminishes the degree of oxygen ordering (Table 1) and impedes the formation of electronic bridges that facilitate the generation of mobile holes. Hence, elevated Tb content further may weaken the coupling mechanism associated with electron-phonon interactions, particularly bipolaron formation within the highly polarizable, strongly covalently bonded Cu-O_2 layers. Structurally, a larger Tb doping level causes more impurity scatterings and disorders in the Y-358 superconducting material, resulting in a broader and less sharp superconducting transition. These results are consistent with the XRD findings, which also show increased impurity phases and structural disorder with higher Tb doping, supporting the conclusion that excessive Tb doping negatively affects the superconducting properties of Y-358. Namely, although this result supports the notion that the incorporation of Tb ions into the crystal lattice does not disrupt the orthorhombic symmetry, it nonetheless deteriorates the basic crystal quality. Based on all the obtained results, it is evident that while the presence of Tb impurities does not significantly alter the phase coherence of the Cooper pair wave function, it does induce a slight reduction in its amplitude. Moreover, it can be stated that all the ceramic samples synthesized in the present study exhibit relatively higher critical transition temperatures (T_c and T_{c0}) compared to those of the Sm-358 and Gd-358 phases, except for the YZ15 and YT15 compositions. Specifically, the Sm-358 sample shows a superconducting onset temperature (T_c) of approximately 65.08 K and a zero-resistance temperature (T_{c0}) of 56.59 K, whereas the corresponding values for the Gd-358 phase are around 76.87 K and 66.23 K, respectively [37].

Figure 6b also presents the ρ–T measurements for Zn-doped Y-358 samples. As the Zn doping level increases, the T_c of the samples drops steadily. As more Zn is added, both T_c^{onset} and T_c^{offset} values become lower, while the transition width gets much wider. For example, the YZ15 sample with the highest Zn content has a very broad transition, with ΔT_c reaching 16.90 K, as presented in Table 3. At the highest Zn doping level, the transition is not only broad but sometimes displays a two-step change, illustrating weak links between grain boundaries. These findings are consistent with the structural analysis and XRD data, which show more disorder as the Zn content increases, especially at 10% and 15% doping levels. This overall trend indicates that higher Zn doping negatively affects the superconducting properties and structural uniformity of the Y-358 superconducting ceramic structures.

A comparative analysis of Tb- and Zn-doped Y-358 ceramic matrices (provided in Fig. 7) demonstrates that both dopants suppress the superconducting transition temperature and broaden the transition width, primarily due to a decrease in the mobile hole carrier concentration involved in the superconducting mechanism, modifications of the

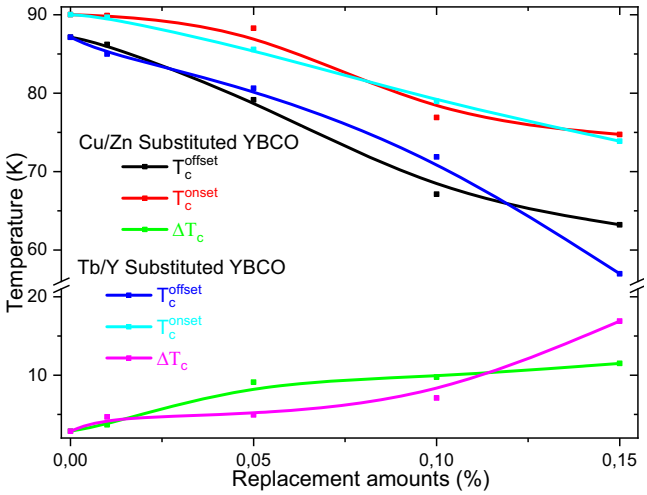


Fig. 7 Change in T_c^{onset}, T_c^{offset}, and ΔT_c parameters against Tb/Y and Cu/Zn partial substitution levels

pseudogap state in high-T_c cuprates [45], and the emergence of charge and spin phase separation phenomena [46]. However, they differ not only in the magnitude of their impact but also in the underlying mechanisms through which they influence superconductivity. Tb^{3+} ions, with a larger ionic radius than Y^{3+}, cause more strain in the crystal lattice, leading to greater disorder and impurity formation. As a result, Tb doping causes a sharper decrease in T_c and a greater broadening in the transition interval after 5% doping, as already verified by SEM, XRD, and M-H experimental results. In contrast, Zn^{2+} ions possess an ionic radius comparable to that of Cu^{2+}, allowing for more seamless integration into the crystal lattice with minimal structural disruption at lower doping levels. However, at higher Zn concentrations, a degradation in superconducting properties is still observed. These findings indicate that although both dopants adversely affect the superconducting performance of Y-358, the extent of structural distortion induced by Tb impurity substitution is more pronounced than that caused by Zn ones. This conclusion is consistent with previous reports in the literature [18].

To sum up, the observed decline in superconducting properties is strongly correlated with variations in phase coherence, orthorhombicity, and doping concentration. This indicates that the introduction of both Tb and Zn impurities and the emergence of structural defects within the orthorhombic framework of the Y-358 superconducting phase significantly influence the critical transition temperatures. Although Y-358 is identified in the literature as a novel high-T_c phase within the YBCO family, reportedly achieving superconductivity above 100 K, many experimental studies, including the present one, have recorded T_c values below 100 K, closely resembling those of the well-known Y-123 phase [12, 47, 48]. This recurring observation supports the hypothesis that the Y-358 phase may, in fact, represent an impurified and defect-laden variant of the Y-123 phase. In other words, despite earlier claims of enhanced superconducting performance, the findings of this study demonstrate that even minimal impurity incorporation is sufficient to destabilize the Y-358 superconducting phase. Based on these valuable results, further research efforts in applied superconductivity should emphasize the need for structural stability and phase purity, especially for technologies reliant on high-performance materials in heavy-industry applications, advanced engineering systems, and large-scale superconducting infrastructure. Ultimately, this study highlights that the substitution mechanism exerts a pronounced influence on the Y-358 phase, due to its sensitivity to changes in orthorhombicity, the emergence of impurity phases, skeleton structure destabilization, crystallographic imperfections, inhomogeneities in oxidation states, degrees of oxygen ordering, and enhanced impurity scattering.

3.4.2 Charge carrier concentrations

The mobile hole concentration (p) within the in-plane Cu–O_2 planes of Y-358 superconductor ceramic structures is critically governed by factors such as oxygen stoichiometry, lattice defects, and elemental substitutions, particularly with dopants like Tb and Zn. Modifications to the oxygen content, the presence of cation vacancies, or the incorporation of dopant ions directly influence the density of mobile holes associated with Cu–O bonding, thereby exerting a significant effect on the superconducting transition temperatures. In particular, the introduction of foreign impurities such as Tb ions tends to reduce the hole concentration p parameter, likely due to enhanced structural disorder and weakened coupling between adjacent Cu–O_2 layers. This reduction in carrier density correlates with a measurable decrease in T_c values. The calculated p values for all Y-358 ceramic matrices are presented in Fig. 8a, b and detailed in Table 3.

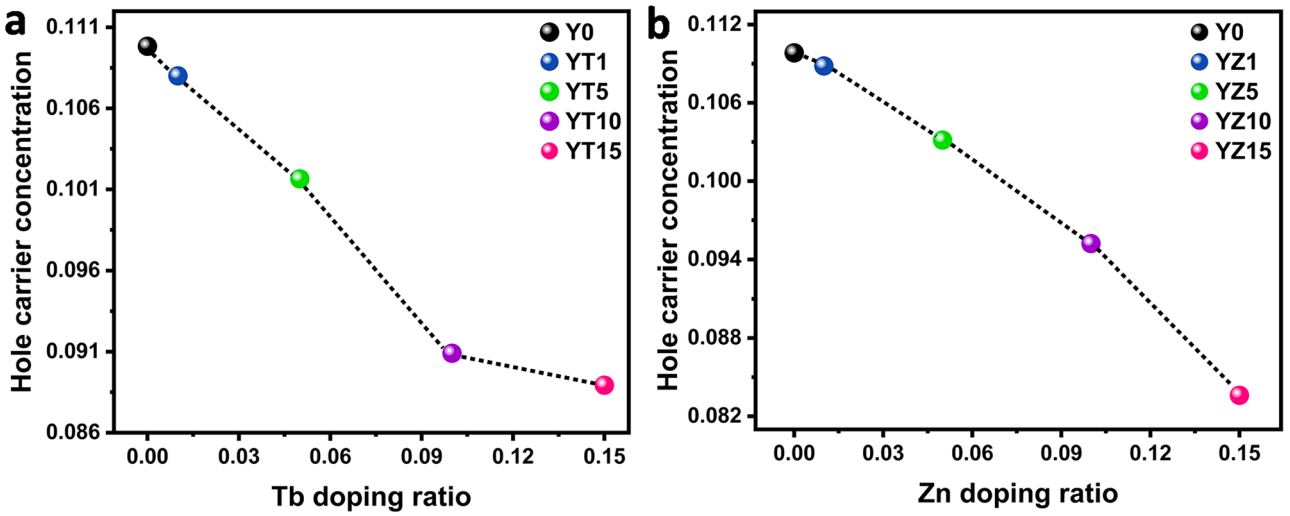


Fig. 8 Mobile hole carrier concentration values of the **a**) Tb-replaced and **b**) Zn-replaced Y358 samples

As shown in Fig. 8a, the p values decrease gradually as the Tb impurity content increases in the Y-358 ceramic structures. The decrement trend is especially pronounced for the samples with 10% and 15% Tb (YT10 and YT15). The substitutions of Tb^{3+} for Y^{3+} ions most likely alter the electronic structure of the conductive Cu–O_2 planes, reducing both the p and T_c parameters. This trend is consistent with resistivity, XRD, and M-H results, which show more impurity phases and lower superconducting transition temperatures for higher Tb impurity contents.

A similar trend is also observed for Zn-doped samples, illustrated in Fig. 8b. Increasing Zn content leads to a drop in the carrier concentration parameter, especially for the YZ15 bulk sample. Although Zn^{2+} ions replace Cu^{2+} and might be expected to add extra electrons, the actual effect is a decrease in mobile holes. This is likely due to increased lattice disorder and disruption of the strongly covalently bonded Cu–O_2 network. The greater the Zn concentration, the more the structure becomes disordered, which reduces carrier mobility and degrades superconducting properties. At the same time, the reduction in mobile hole carrier concentration results in an increased fraction of stacking faults, enhanced oxygen deficiency, and overall microstructural degradation. These effects are accompanied by a proximity-induced suppression of the superconducting order parameter between inequivalent Cu-O_2 planes and a consequent weakening of the interlayer (c-axis) coupling [26, 49, 50]. In fully oxygenated YBCO, strong overdoping further illustrates this mechanism, with Tc being markedly suppressed. Notably, the phenomenon is governed more by generic electronic phase (spin) separation than by oxygen-vacancy ordering, highlighting the role of nanoscale electronic inhomogeneity in dictating superconducting behavior. Moreover, the reduction of tanstion temperature under Zn substitution is consistent with unitarity-limit scattering of quasiparticles in a d-wave superconductor in the presence of a pseudogap [26]. At higher substitution levels, these effects drive the system toward a spin-glass–like phase, where superconductivity and short-range antiferromagnetism coexist and compete [45].

Moreover, the different charge, ionic radius, and electronic configuration of Zn^{2+} particles compared to Cu^{2+} ions cause further structural disorder, resulting in lower carrier concentration. A detailed analysis is presented in the subsequent sections. Both Tb and Zn dopants contribute to a reduction in the p value within Y-358 ceramic structures; however, the decline induced by Tb impurities is more significant and becomes increasingly pronounced at higher doping levels, particularly beyond the 5% substitution threshold. In contrast, Zn/Cu partial substitution results in a more gradual and nearly linear decline in p across the studied doping range. The sharper decrease in p parameter for Tb-doped Y-358 ceramic structures is attributed to the larger ionic size of Tb^{3+} impurity ions and the greater lattice strain and disorder it introduces, which more severely disrupts the adjacent conductive Cu–O_2 planes. The reductions in p parameter are consistent with the observed decrease in T_c values and align with previous findings linking structural distortions to weakened superconducting behavior.

3.5 Magnetic behaviors

3.5.1 M-H experimental results

Magnetization hysteresis curves are plotted for the Tb-doped and Zn-doped Y-358 ceramic samples at 20 K, measured under magnetic fields ranging from −2 T to +2 T in Fig. 9a, b, respectively. As seen from the plots, the

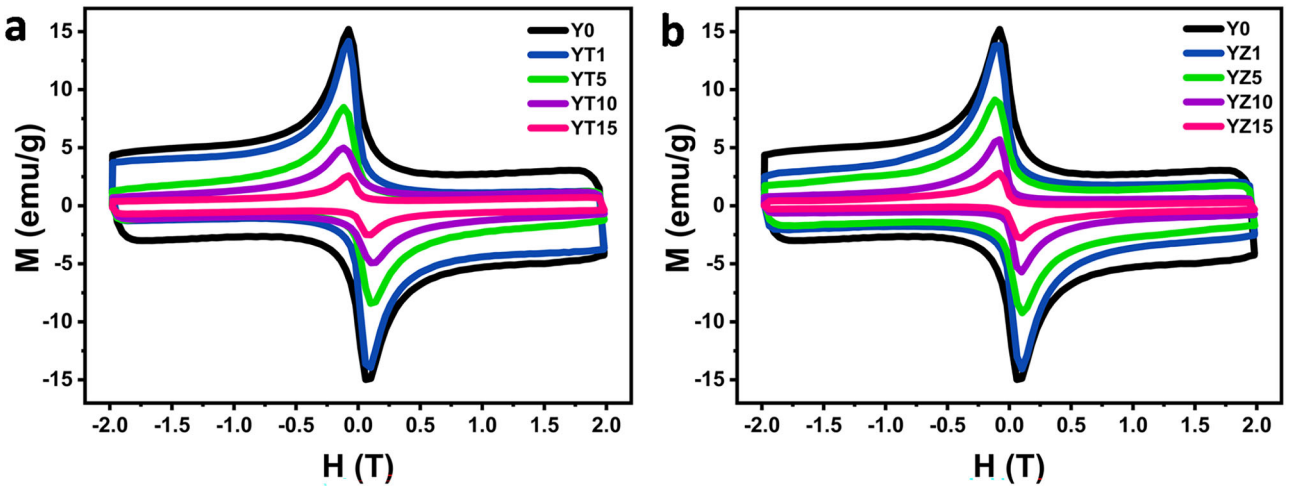


Fig. 9 Magnetization hysteresis loops at 20 K for **a**) Tb-doped and **b**) Zn-doped Y358 samples

magnetization behavior deduced from the area under the hysteresis curves of both series is negatively affected depending on the increase in the impurity percentage, and therefore, the widths of the magnetization loops generally decrease with increasing doping ratio. Any change in the widths of the cycle curves results from the differentiation in the coherence length, flux pinning force, crystallinity quality, interaction quality between grains, and the existence of secondary or unwanted phases [51–54]. In the current work, the figures indicate a serious weakening of the diamagnetic response and a reduction in magnetic flux pinning capacity to the applied magnetic field strengths for both series. The similar trend for the magnetic fluctuations was observed for the $TR_3Ba_5Cu_8O_\delta$ (where TR=Ho, Y and Yb) superconducting systems [10].

In more detail, according to Fig. 9a, the pristine Y0 sample exhibits the largest magnetic moment and loop area, indicative of stronger magnetic flux pinning and higher superconducting volume fraction. In this context, the SG preparation technique was employed to synthesize ceramic materials with tailored structural and functional properties.

With the progressive substitution of Tb^{3+} ions for Y^{3+} sites in the Y-358 ceramic structure, the magnetic hysteresis loop area becomes narrower, and the magnetization decreases significantly. The decrement trend also stems from the fact that the partial substitution introduces local magnetic inhomogeneities, disrupting the superconducting pathways. In particular, the YT10 and YT15 samples show significant narrowing of the loops and lower magnetization saturation levels, indicating increased flux mobility, weaker intergranular coupling, and enhanced structural disorder. These effects are likely due to Tb-induced lattice strain, impurity phases that hinder effective superconducting current paths as evident from the shrinking loop width and magnetization.

As for the magnetic behavior of Zn-doped Y-358 samples, similarly, increasing Zn concentration leads to a gradual narrowing of the hysteresis loops and symmetrically reduced magnetization, as seen in Fig. 9b. However, the decline is more gradual compared to Tb doping, and the magnetic response remains relatively symmetric and broader even at 15% Zn content. The observed reduction in magnetic performance is attributed to increased lattice defects and weakened coherence between superconducting grains caused by Zn substitution, which disrupts the adjacent conductive Cu–O_2 network and flux pinning. Namely, Zn substitution introduces non-superconducting regions that reduce the effective cross-section for current flow, weakening intergrain connectivity.

Both Tb and Zn dopants weaken the magnetic response and diminish the diamagnetic effect in Y-358 superconductors, as evidenced by the narrowing M–H loops and lower magnetization values. However, the weakening is more pronounced at higher doping levels, particularly for Tb impurities. This difference can be attributed to the larger ionic size and stronger lattice distortions caused by Tb ions, leading to more severe grain boundary and impurity effects compared to Zn ones. Both types of doping disrupt the superconducting phase due to the induced new lattice strains and distorted Cu–O planes, but the mechanism and extent of the magnetic degradation are related to the dopant's nature and concentration. Besides, the changed hole doping levels with the partial substitutions in the Cu–O planes, indirectly weakening the superconducting order parameter. Moreover, M–H curves are used to discuss the variation of coercivity, remanent magnetization, critical current density, pinning force mechanism in the Y-358 crystal matrix with substitution mechanism.

In Fig. 9a, b, the point where the hysteresis loop crosses the H-axis is coercivity. As seen from the plots, all samples

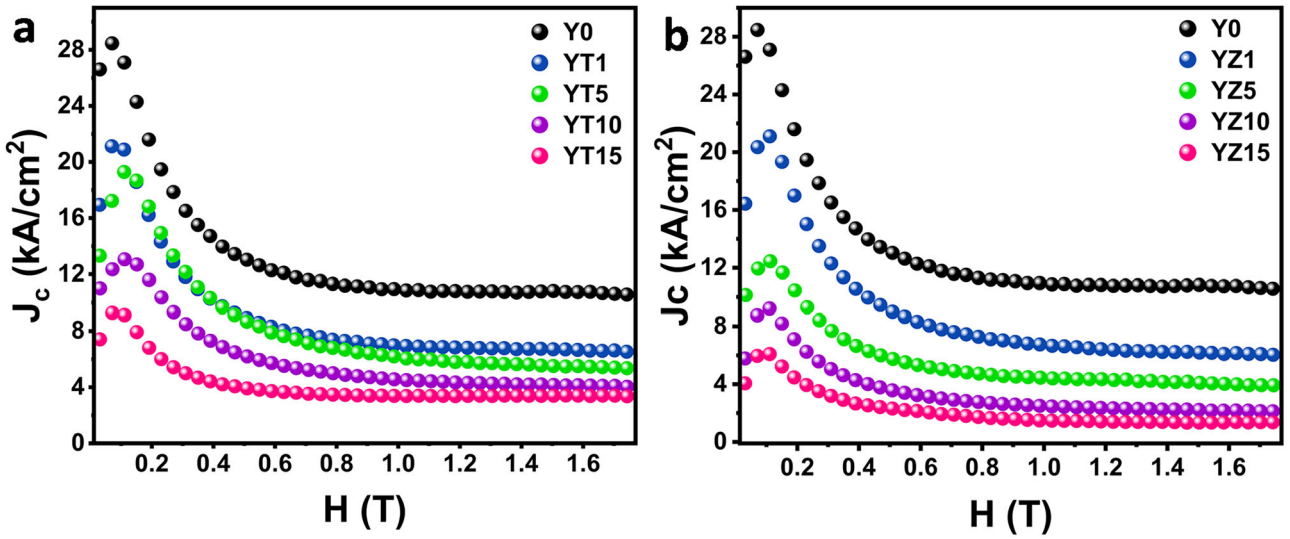


Fig. 10 Critical current density of **a**) Tb-doped and **b**) Zn-doped Y358 samples

prepared exhibit symmetrical hysteresis loops due to their soft magnetic behavior. For both series, Y0 ceramic samples present the widest separations between the zero-magnetization points related to the highest coercivity. Accordingly, the materials indicate much stronger vortex pinning and better superconducting integrity. On the increase in the impurity ions in the Y-358 ceramics, the loops become narrower and thus coercivity decreases considerably as a result of the increased structural and electronic disorders, indicating weaker pinning ability and reduced magnetic irreversibility and coercivity. Likewise, the sol–gel synthesized pristine Y0 ceramics possess the highest remanent magnetization, indicating strong persistent currents and robust superconductivity. With increasing foreign impurity ions, remanent magnetization values decrease systematically and reach the global minimum values for the highest substitution level. On this basis, among the groups both YT15 and especially YZ15 show much lower remanent magnetization, implying weaker superconducting flux pinning.

3.5.2 Critical current density

The critical current density (J_c), indicating the maximum current the material can carry without resistance is a key parameter for technological applications of copper-based superconductors like YBCO. The J_c parameter is strongly governed by the microstructural characteristics, the density and distribution of flux pinning centers, and the phase purity of the ceramic matrix. Similar to the superconducting transition temperature, the critical current density in YBCO ceramics exhibits a pronounced dependence on the mobile charge carrier concentration [49]. In turn, p is directly influenced by the oxygen content (δ) and the efficiency of charge transfer between the Cu-O chains and Cu-O_2 planes, which collectively determine the superconducting performance of the system.

Hence, J_c can be enhanced by increasing the flux pinning ability, which relies on the effectiveness of pinning centers that trap magnetic flux lines when the applied magnetic field exceeds H_{c1} [10, 55, 56]. The variation of J_c with magnetic field is analyzed using Bean's critical state model [33], where the width of the M–H curves directly reflects J_c values. Therefore, changes in the hysteresis loop width provide important information about the material's ability to carry current under a magnetic field. Correspondingly, the critical current density values and pinning force values calculated using ΔM values are also parallel to the obtained results, as expected.

Figure 10a shows the field dependence of J_c for the undoped and Tb-doped Y-358 samples at 20 K. The Y0 exhibits the highest J_c values across all applied fields. All synthesized samples exhibit a high current-carrying capacity, arising from their intrinsic superconducting nature and efficient charge transport mechanisms. This performance is further attributed to the targeted crystalline quality and uniform compositional homogeneity achieved through the sol–gel method, a superior, effective, and reliable synthesis route for producing advanced high-performance ceramic systems. As the Tb doping level increases, the J_c values decrease systematically, and this reduction is especially significant at higher Tb concentrations (10% and 15%). This means that the ability of the material to carry high current under a magnetic field becomes weaker with more Tb impurity ions in the ceramic matrix. The main cause of the decrement trend is the negative effect of Tb ions on the

nucleation centers serving as effective flux pinning regions in the material. Increased Tb doping introduces more defects, impurities, and smaller grains, all of which weaken the flux pinning capability and interlayer Josephson coupling between the stacked adjacent layers. As a result, magnetic flux lines (thermal fluxon motions of 2D pancake vortices) begin to move more easily, leading to a rapid decrease in the J_c parameter. According to a previous publication [18], higher Tb substitution also causes a reduction in the energy barriers for thermal flux motion and increases structural disorder, which further limits the superconducting performance.

Figure 10b also presents the J_c values for Zn-doped Y-358 samples. Similar to the Tb-substituted Y-358 ceramic samples, the Y0 shows the highest J_c values, and increasing Zn content leads to a rapid decrease in J_c for all samples. The effect is most obvious at higher Zn doping levels (YZ10 and YZ15). This drop in J_c value can be explained by the increased number of defects and impurities in the microstructure, resulting in degradation of interlayer connection strengths throughout the grain boundaries. In this respect, increased imperfections based on excess Zn impurity content disrupt the structure, weaken flux pinning centers, and make it harder for the superconductor to maintain high current densities in a magnetic field application. Additionally, the difference in charge and ionic size between Zn^{2+} and Cu^{2+} generates more structural disorder, leading to a greater reduction in the potential energy barriers, effectiveness of flux pinning, and lower J_c values.

Comparative analysis reveals that both Tb and Zn doping reduce the J_c parameter of Y-358 superconductors by disrupting the flux pinning mechanism and increasing the number of structural defects [57]. Similarly, the presence of impurity ions facilitates the recoupling of linear or discrete pancake-like vortex structures. As a result, the flux lines generated by the external magnetic field within ceramic superconductors are more likely to hop between adjacent pinning sites, thereby enhancing the likelihood of Cooper pair breaking. Consequently, energy dissipation occurs rapidly due to the thermally activated motion of two-dimensional discrete pancake vortices. However, the reduction is more severe in Tb-doped samples, likely due to the larger ionic radius of Tb^{3+} and its more pronounced impact on the crystal lattice, grain boundaries, and phase homogeneity. This observation explains why the Y-358 superconducting phase with the highest level of Tb substitution exhibits the lowest resistance to externally applied magnetic fields. These results emphasize the importance of carefully controlling dopant type and concentration to preserve superconducting performance. Excessive doping not only reduces grain connectivity but also promotes defect accumulation, ultimately leading to a substantial decline in J_c value.

3.5.3 Pinning force mechanism

The width of the magnetization hysteresis curves is directly related to the magnetic flux density entering the superconducting sample, which affects both the J_c and F_p parameters. As fluxons vibrate and move more easily, the diamagnetic effect and pinning ability of the superconductor decrease, especially in samples with increased Tb or Zn doping levels in the main superconducting matrices. Thus, analyzing the width, area, and shape of these loops helps determine how doping alters the magnetic field dependence of J_c and F_p quantities, and these changes generally follow the observed trends in magnetization.

Figure 11a presents the normalized pinning force (F_p/F_{pmax}) versus reduced field (H/H_{max}) for Tb-doped Y-358 ceramic superconductors. As the Tb content rises, F_p values decrease regularly due to the decrease in the nucleation centers (interlayer Josephson couplings) and related pinning capacity. As observed in previous M–H and J_c results, the narrowing of the hysteresis loops with excess Tb impurity confirms this situation. The decreasing trend observed in the F_p is attributed to the increased concentration of impurities, enhanced lattice strain and particularly the nanoscale nature of Tb ions. These factors collectively promote flux creep and compromise the stability of the superconducting phase. At the same time, the decreased average grain size growth and increased crystal structural problems, lattice strain fields, and grain boundaries impair the pinning force mechanism of the Y-358 ceramic system, as verified by XRD patterns and SEM pictures. According to theoretical analysis, the best fit at low magnetic fields is with the normal point pinning model, while at higher fields, the $\Delta\kappa$ pinning model is more applicable. This is attributed to the fact that most pinning centers in these samples are due to local impurity or defect zones rather than strong, well-distributed nanoscale pinning sites. The instability and structural inhomogeneity observed in XRD and SEM images further support these findings. In summary, higher Tb doping increases structural defects and disorder, reduces the effectiveness of pinning centers, and weakens the ability of the superconductor to trap magnetic flux lines, leading to lower J_c and poorer superconducting performance.

Figure 11b shows the normalized pinning force for Zn-doped Y-358 samples as a function of field. Here, increasing Zn content results in a decrease in F_p parameter, confirming that Zn is also not effective in forming strong flux pinning centers. The trend matches the observed decline in both magnetization and critical current density with more Zn impurity doping. Similar to Tb ions, the main pinning mechanism at low magnetic fields is best described by the normal point pinning model, while the $\Delta\kappa$ model fits better at higher fields. This indicates that impurity zones act as pinning points, but these are neither strong nor well-

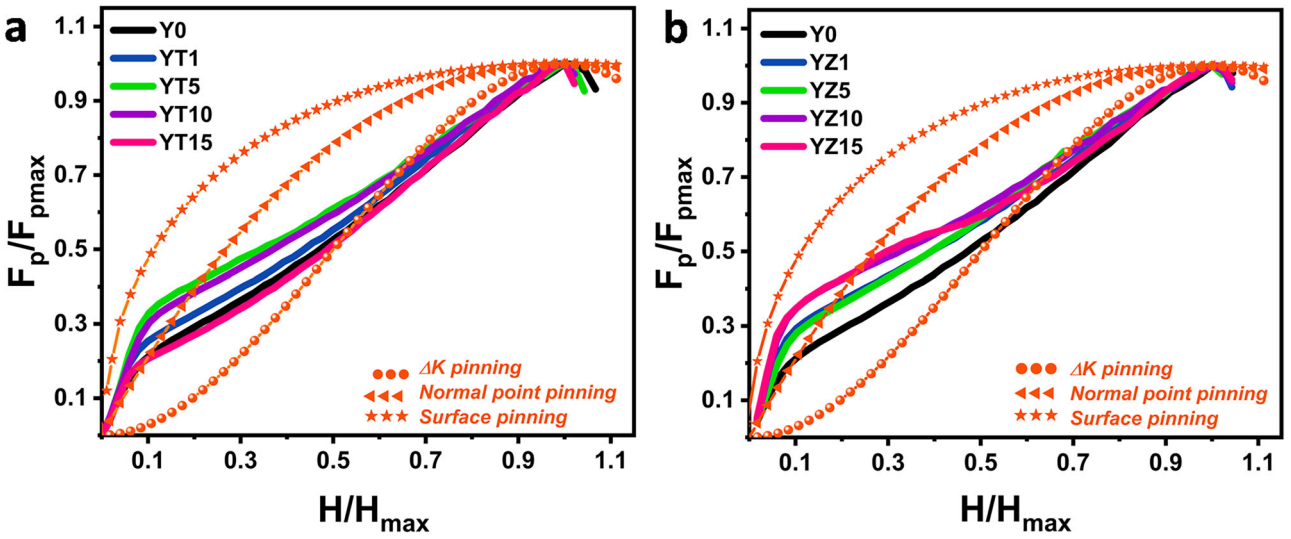


Fig. 11 Normalized flux pinning force (F_p/F_{pmax}) as a function of reduced magnetic field (H/H_{max}) at 20 K for **a**) Tb-doped and **b**) Zn-doped Y358 samples

organized enough to offer robust flux trapping, particularly as doping increases. The different charge and ionic radius of Zn^{2+} compared to Cu^{2+} increase local disorder, reduce homogeneity, and limit the formation of efficient pinning centers. Regardless, the SG method demonstrates significant effectiveness as a versatile and reliable technique for the synthesis of high-quality ceramic materials.

Comparative analysis reveals that the presence of foreign impurities remarkably harms the nucleation centers (inter-layer Josephson couplings), impairs the pinning force capacity for the thermal fluxon motions of 2D pancake vortices, and pinning force ability based on the instability of the characteristic Y-358 superconducting phase, which is already supported by the result of XRD and electrical resistivity measurements. Especially, the reduction in F_p values with increasing dopant concentration is more severe in Tb-doped samples than in Zn-doped ones. This is attributed to the larger ionic radius of Tb^{3+}, and its stronger impact on lattice strain and structural inhomogeneity. While both dopants reduce the effective flux pinning areas, the effect of Tb impurity is more detrimental, leading to enhanced flux creep and degraded superconducting performance. According to the applied theoretical models, the presence of nanoscale impurities, oxygen deficiency, and poorly connected grain structures further limits the distribution of nucleation centers in both systems, with these factors being especially pronounced in the Tb-substituted Y-358 ceramic series [34, 58, 59].

4 Conclusion

In this comprehensive study, the influence of partial substitution of trivalent Tb^{3+} at Y^{3+} sites and divalent Zn^{2+} at Cu^{2+} sites on the structural, microstructural, electrical, and magnetic characteristics of Y-358 high-temperature superconducting ceramics is rigorously investigated. The experimental results reveal that incorporating both Tb and Zn impurity ions significantly alters the intrinsic properties of the Y-358 ceramic system, albeit through distinct mechanisms and to differing extents. This shows that the materials are synthesized with the targeted crystalline quality and compositional homogeneity, meaning that achieving ceramic materials with the desired crystalline quality highlights the sol–gel method as a highly effective and reliable synthesis route for the preparation of advanced, high-performance ceramic systems. XRD analyses indicate that both dopants affect phase stability, lattice strain, crystallinity quality, and unit cell dimensions. However, Tb substitution introduces more pronounced structural disruptions and impurity phase formation, such as $BaTbO_3$ and $BaCuO_2$, compared to Zn impurity, which demonstrates better lattice compatibility at low-to-moderate doping levels. These structural modifications are indicative of increased orthorhombic-to-tetragonal distortions, with Tb doping severely disturbing the Cu-O_2 interlayer coupling strength and integrity, a key feature in sustaining superconductivity.

SEM imaging, corroborated by histogram-based grayscale analysis and particle size evaluations, provides further valuable information about the dopant-induced morphological changes. Tb^{3+} impurities result in irregular, porous microstructures with high grain boundary density and reduced grain connectivity, particularly at higher substitution levels of $x = 0.10$ and $x = 0.15$. In contrast, Zn-doped samples exhibit finer, more uniformly distributed grains and a relative improvement in surface morphology, especially at

intermediate concentrations, displaying that Zn plays a more constructive role in facilitating controlled grain refinement and surface densification. EDX analyses verified the effective incorporation of Tb and Zn dopants through the substitution of Y and Cu sites, respectively, within the Y-358 ceramic lattice, indicating that the dopant-induced modifications significantly influence microstructural uniformity and the continuity of superconducting current pathways, either enhancing or degrading them depending on dopant concentration.

Electrical transport measurements confirm that both Tb and Zn impurity substitutions degrade the superconducting properties of Y-358, manifested through decreased superconducting transition temperatures, increased transition widths, and elevated normal-state resistivity. These effects are attributed to reduced mobile hole concentration within the Cu-O_2 planes, lattice-induced electronic disorder, perturbations of the pseudogap state, and disruption of oxygen ordering, spin (phase) separation, and electronic density of states. Tb impurity replacement, in particular, leads to a more abrupt decline in T_c parameters and carrier density, consistent with its stronger influence on structural distortion and electronic inhomogeneity.

Magnetization measurements under varying magnetic fields reveal a pronounced deterioration in the flux pinning capacity and critical current density with increasing dopant content. The M-H hysteresis loops narrow significantly for Tb-replaced Y-358 superconducting ceramics, indicating weakened flux pinning, increased flux creep, and reduced superconducting volume fraction. Zn impurity also leads to reduced J_c value; however, the decline is less severe and more gradual, maintaining relatively better magnetic performance at moderate concentrations. The normalized pinning force analyses indicate that flux pinning in both substituted ceramic systems primarily follows a normal point pinning mechanism at low fields and shifts to $\Delta\kappa$-type pinning at higher fields, pointing to impurity- and defect-driven artificial pinning sites.

In summary, while the presence of both Tb and Zn impurities negatively impacts the superconducting phase integrity and performance of Y-358 ceramics, the extent and nature of these effects vary considerably. Tb^{3+} foreign ions, due to their larger ionic radius and stronger propensity to disrupt the crystal lattice, induce more substantial structural instability, phase impurity formation, and grain connectivity degradation, resulting in a steeper decline in superconducting and magnetic properties. Zn^{2+} impurity ions, by contrast, exhibit more favorable substitution behavior, allowing for improved grain refinement and surface uniformity at optimized concentrations, though higher Zn levels still introduce detrimental effects.

All the obtained results emphasize the critical importance of dopant selection and concentration control in preserving the structural coherence, phase homogeneity, and functional integrity of high-T_c superconducting ceramic structures. The sensitivity of the Y-358 superconducting phase to even moderate levels of impurity highlights the necessity of precise synthesis strategies and post-processing protocols in applications requiring reliable and efficient superconducting behavior. This investigation offers valuable insights for the strategic design and optimization of doped Y-based superconductors, with potential implications for their deployment in advanced magnetoelectronic systems, power transmission technologies, and energy storage applications.

Data availability

No datasets were generated or analysed during the current study.

Code availability

The datasets used or analyzed during the current study are available from the corresponding author on reasonable request.

Author contributions G.G., O.O., S.K. and T.S. conceived the idea for the project and designed the experiments. T.S., G.Y., A.S.E., and E.A.T. performed methodology, project administration, investigation also performed materials production. G.Y., S.S., O.O., S.K., and E.A.T. performed experimental measurement and resources, formal analysis, review & editing. A.S.E., E.A.T., O.O., and G.Y. performed writing - original draft, writing - review & editing. All authors discussed the results and commented on the manuscript.

Funding This research did not receive any specific grant from funding agencies in the public, commercial, or not-for-profit sectors. Open access funding provided by the Scientific and Technological Research Council of Türkiye (TÜBİTAK).

Compliance with ethical standards

Conflict of interest The authors declare no competing interests.

Ethical approval There is no action that requires ethics committee approval.

Publisher's note Springer Nature remains neutral with regard to jurisdictional claims in published maps and institutional affiliations.

Open Access This article is licensed under a Creative Commons Attribution 4.0 International License, which permits use, sharing, adaptation, distribution and reproduction in any medium or format, as long as you give appropriate credit to the original author(s) and the source, provide a link to the Creative Commons licence, and indicate if changes were made. The images or other third party material in this article are included in the article's Creative Commons licence, unless indicated otherwise in a credit line to the material. If material is not included in the article's Creative Commons licence and your intended use is not permitted by statutory regulation or exceeds the permitted use, you will need to obtain permission directly from the copyright holder. To view a copy of this licence, visit http://creativecommons.org/licenses/by/4.0/.

References

1. Duzgun I (2018) The investigation of the lattice strains and crystallite sizes of Y358 and Y123 high-temperature superconductors, Turkish. J Phys 42:378–385
2. Gholipour S, Daadmehr V, Rezakhani AT, Khosroabadi H, Shahbaz Tehrani F, Hosseini Akbarnejad R (2012) Structural Phase of Y358 Superconductor Comparison with Y123. J Supercond Nov Magn 25:2253–2258
3. Basoglu M, Duzgun I, Ozturk A (2021) Specification of Some Superconductivity Parameters by Adding Lutetium to the YBCO (358) Ceramic Superconductor. J Supercond Nov Magn 34:1077–1084
4. Khosroabadi H, Rasti M, Akhavan M (2014) Structural analysis of $Y_3Ba_5Cu_8O_{19-\delta}$ high-T_c superconductor by ab initio density functional theory. Phys C 497:84–88
5. Sangchaisri S, Longhan N, Kruaehong T (2017) Investigation of Superconductivity and Crystal Structure of Y123, Y358 and Y3-8-11 Prepared by Solid State Reaction and Melt Process. J Mater Sci Appl Energy 6(3):233–237
6. Sujinnapram S, Udomsamuthirun P, Kruaehong T, Nilkamjon T, Ratreng S (2011) XRD spectra of New YBaCuO superconductors. Bull Mater Sci 34(5):1053–1057
7. Aliabadi A, Akhavan Farshchi Y, Akhavan M (2009) A new Y-based HTSC with T_c above 100 K. Phys C 469:2012–2014
8. Slimani Y, Hannachi E, Ben Salem MK, Hamrita A, Varilci A, Dachraoui W, Ben Salem M, Ben Azzouz F (2014) Comparative study of nano-sized particles $CoFe_2O_4$ effects on superconducting properties of Y-123 and Y-358. Phys B 450:7–15
9. Slimani Y, Hannachi E, Ben Azzouz F, Ben Salem M (2018) Impact of planetary ball milling parameters on the microstructure and pinning properties of polycrystalline superconductor $Y_3Ba_5Cu_8O_y$. Cryogenics 92:5
10. Topal U, Akdogan M, Ozkan H (2011) Electrical and structural properties of $RE_3Ba_5Cu_8O_{18}$ (RE = Y, Sm and Nd) superconductors. J Supercond Nov Magn 24:2099–2102
11. Ayas AO, Ekicibil A, Cetin SK, Coskun A, Er AO, Ufuktepe Y, Fıirat T, Kiymac K (2011) The structural, superconducting and transport properties of the compounds $Y_3Ba_5Cu_8O_{18}$ and $Y_3Ba_5Ca_2Cu_8O_{18}$. J Supercond Nov Magn 24:2179
12. Barakat M, Abou-aly A, Awad A, Aly N, Ibrahim S (2015) Mechanical properties of $Y_{3-x}Nd_xBa_{5-x}Ca_xCu_8O_{18-\delta}$ samples. J Alloy Comp 652:158
13. Esmaeili A, Sedghi H, Golzan MM, Amniat-Talab M (2011) The Normal State Properties of $Y_3Ba_5Cu_{8-x}Zn_xO_{18-\delta}$ Superconductor in Bipolaron Model. J Supercond Nov Magn 24:2237–2242
14. Metin T, Tepe M (2017) The Effect of Ag Doping on the Superconducting Properties of $Y_3Ba_5Cu_{8-x}Ag_xO_{18-\delta}$ Ceramics. J Supercond Nov Magn 30:1083–1087
15. Udomsamuthirun P, Kruaehong T, Nikamjon T, Ratreng S (2010) The new superconductors of YBaCuO materials. J Supercond Nov Magn 23:1377–1380
16. Tavana A, Akhavan M (2010) How T_c can go above 100 K in the YBCO family. Eur Phys J B 73:79–83
17. Ozturk O, Arebat RAM, Nefrow ARA, Bulut F, Guducu G, Asikuzun E, Celik S (2019) Investigation of structural, superconducting and mechanical properties of Co/Cu substituted YBCO-358 ceramic composites. J Mater Sci: Mater Elect 30:7400–7409
18. Guducu G, Ozturk O, Kurnaz S, Tokeşer EA, Safran S, Yıldırım G (2024) Assessment of superconducting and structural stability of advanced Y-123 and Y-358 ceramics with Tb/Y substitution in main matrices. J Alloy Comp 997:174838
19. Ozturk O, Guducu G, Kurnaz S, Seydioğlu T, Safran S (2025) Structural and Mechanical Dynamics of Y-358 Superconductors Influenced by Tb/Y and Zn/Cu Substitutions. J Supercond Nov Magn 38:38
20. Tampieri A, Celotti G, Lesca S, Bezzi G, La Torretta TMG, Magnani G (2000) Bi(Pb)–Sr–Ca–Cu–O (2223) superconductor prepared by improved sol–gel technique. J Eur Ceram Soc 20(2):119–126
21. AR West, (2022). Solid state chemistry and its applications. John Wiley & Sons
22. E Asikuzun, G Yildirim, AS Erturk, et al. Role of Mg substitution in modulating defect-mediated magnetism and mechanical strength of $Zn_{0.95}Co_{0.0}5O$ systems. J Sol-Gel Sci Technol (2025). https://doi.org/10.1007/s10971-025-06882-7
23. Kurtul G, Ulgen AT, Armagan O, Turkoz MB, Erdem U, Yildirim G (2025) Role of dysprosium substitution on microscopy architecture, structural stability, and crack propagation mechanism in Bi-2212 engineering ceramics. Phys Scr 100(2):025932
24. Yildiz A, Kocabas K, Akyuz GB (2012) J Supercond Nov Magn 25:1459–1467
25. BD Cullity, Elements of X-ray Diffraction, third ed., Addition-Wesley, Reading, 2001.
26. Tallon JL, Bernhard C, Shaked H, Hitterman RL, Jorgensen JD (1995) Generic superconducting phase behavior in high-T, cuprates: T, variation with hole concentration in $YBa_2Cu_30_{7-\delta}$. Phys Rev B 51:12911–12914
27. Tallon JL, Loram JW (2001) The doping dependence of T* – what is the real high-Tc phase diagram?. Phys C: Superconductivity 349(Issues 1–2):53–68
28. Stangl A, Palau A, Deutscher G et al. (2021) Ultra-high critical current densities of superconducting $YBa_2Cu_3O_{7-\delta}$ thin films in the overdoped state. Sci Rep 11: 8176
29. Naqib SH, Islam RS (2019) Possible quantum critical behavior revealed by the critical current density of hole doped high-T_c cuprates in comparison to heavy fermion superconductors. Sci Rep 9: 14856
30. Presland MR, Tallon JL, Buckley RG (1991) Flower, General trends in oxygen stoichiometry and T_c in Bi and Tl cuprate superconductors. Phys C: Superconductivity 176:95–105
31. Terzioglu R (2021) Evaluation of magnetotransport properties of Au added YBCO ceramics: combination of experimental and advanced theoretical approaches. J Mater Sci: Mater Electron 32:4737–4748
32. Erdem U, Turkoz MB, Yildirim G, Zalaoglu Y, Nezir S (2021) Refinement of fundamental characteristic properties with homovalent Er/Y partial replacement of $YBa_2Cu_3O_{7-y}$ ceramic matrix. J Alloy Comp 884:161131
33. Bean CP (1964) Magnetization of high-field superconductors. Rev Mod Phys 36:31–39
34. Higuchi T, Yoo SI, Murakami M (1999) Comparative study of critical current densities and flux pinning among a flux-grown $NdBa_2Cu_3Oy$ single crystal, melt-textured Nd-Ba-Cu-O, and Y-Ba-Cu-O bulks. Phys Rev B 59:1514
35. Chaillout C, Bordet P, Chenavas J, Hodeau JL, Marezio M, Karpinski J, Kaldis E, Rusiecki S (1989) Electron microscopy study of the new high Tc phase $Y_2Ba_4Cu_7O_{14+x}$. Solid State Commun 70:275–278
36. Hamrita A, Azzouz FB, Madani A, Salem MB (2012) Magnetoresistivity and microstructure of $YBa_2Cu_3O_y$ prepared using planetary ball milling. Phys C 472:34–38
37. Camarga CCC et al. (2025) Evaluation of the structural, morphological, and magnetic properties of the RE-358, RE-123, RE-$Ca_{0.1}$ with RE= Gd and Sm superconductors. Phys C: Superconductivity its Appl 630:1354647
38. Topal U, Akdogan M (2011) Further increase of T_c in Y-Ba-Cu-O superconductors. J Supercond Nov Magn 24:1815–1820
39. Gaona IMS, Supelano GI, Vargas CAP (2020) Determination of critical superconducting parameters based on the study of the magnetization fluctuations for $RE_3Ba_5Cu_8O_{18-y}$ (RE= Sm, Eu, Gd, Dy and Ho) ceramic superconductor system. Ceram Int 46(no 8):11530–11538

40. Supelano GI, Sarmiento AS, Vargas CAP (2014) Magnetic fluctuations on $TR_3Ba_5Cu_8O_y$ (TR=Ho, Y and Yb) superconducting system. Phys B: Condens Matter 455:79–81
41. Bibekananda S, Krutika LR, Bandana P, Samal D, Dhrubananda B (2019) Excess conductivity and magnetization of $CoFe_2O_4$ combined with $YBa_2Cu_3O_{7-d}$ as a superconductor. J Phys Chem Solids 132:187
42. Dynes RC, White AE, Graybeal JM, Garno JP (1986) Breakdown of Eliashberg theory for two-dimensional superconductivity in the presence of disorder. Phys Rev Let 57:2195–2198
43. Akkurt B, Erturk AS, Erdem U, Turgay T, Yildirim G (2025) Bridging key mechanical performance and electrical-superconducting functionalities in Na ion-added Bi-2212 engineering Ceramics: Underlying crystal defect mechanisms. Ceram Int 51:36359–36374
44. Saleh SA, Ahmed SA, Elshikh EMM (2008) A Study on Thermoelectric Power and Electrical Properties of Bi-2223 Superconductors Sintered for Different Time Periods. J Supercond Nov Magn 21:187–192
45. Tallon JL, Williams GVM, Flower NE, Bernhard C (1997) Phase separation, pseudogap and impurity scattering in the HTS cuprates. Phys C: Supercond 282 287:236–239
46. Akoshima M, Koike Y, Watanabe I, Nagamine K (2000) Anomalous muon-spin relaxation in the Zn-substituted $YBa_2Cu_{3-2y}Zn_{2y}O_{7-\delta}$ around the hole concentration of 1/8 per Cu. Phys Rev B 62:6761–6765
47. Esmaeili A, Sedghi H, Golzan MM, Amniat-Talab M (2011) The normal state properties of $Y_3Ba_5Cu_{8-x}Zn_xO_{18-\delta}$ superconductor in bipolaron model. J Supercond Nov Magn 24:2237–2242
48. Akyol M, Ayas AO, Akça G, Cetin SK, Ekicibil A (2015) Effect of Ca doping on thermally activated flux flow in the $Y_3Ba_5Cu_8O_{18}$ superconductor. Bull Mater Sci 38(5):1231–1237
49. Talantsev EF, Strickland NM, Wimbush SC, Storey JG, Tallon JL, Long NJ (2014) Hole doping dependence of critical current density in $YBa_2Cu_3O_{7-\delta}$ conductors. Appl Phys Lett 104:242601
50. Obertelli SD, Cooper JR, Tallon JL (1992) Phys Rev B 46:14928
51. Hannachi E, Almessiere MA, Slimani Y, Baykal A, Ben Azzouz F (2020) AC susceptibility investigation of YBCO superconductor added by carbon nanotubes. J Alloy Comp 812:152150
52. Wei K, Abd-Shukor R (2007) Superconducting and transport properties of (Bi–Pb)–Sr–Ca–Cu–O with nano-Cr2O3 additions. J Elect Mater 36:1648–1651
53. Slimani Y, Hannachi E, Ekicibil A, Almessiere MA, Azzouz FB (2019) Investigation of the impact of nano-sized wires and particles TiO_2 on Y-123 superconductor performance. J Alloy Comp 781:664–673
54. Kara E, Dogan MU, Kaya S, Terzioglu R, Yildirim G, Terzioglu C (2023) Evolution of basic features of $Bi_{1.8}Pb_{0.4}Sr_2Ca_{2.2}Cu_3O_y$ ceramic systems with NiO impurity. J Mater Sci: Mater Elect 34:1483
55. Ozturk A, Duzgun I, Basoglu M, Celebi S (2019) Comparative Investigation on Magnetic Behavior of Partial Rare Earth Element (Re: Lu, Yb, and Dy) Substituted $Y_{0.5}Re_{0.5}$BCO (123) Superconductors. J Supercond Nov Magn 33:583–590
56. El-Aziz A, Ahmed M, Afifi HA, Hager IZ, Abdel Aal NS, Naqib SH (2019) Unusual Enhancement of Normal and Superconducting State Properties of (100-x)$YBa_2Cu_3O_{7-\delta}$ + xNi (x = 1, 2.5, 5, 7.5, 10, and 15 wt%) Composites with Low Level of Ni Additives. J Supercond Nov Magn 33:661–674
57. Slimani Y, Hannachi E, Hamrita A, Ben Salem MK, Ben Azzouz F, Manikandan A, Ben Salem M (2018) Comparative investigation of the ball milling role against hand grinding on microstructure, transport and pinning properties of $Y_3Ba_5Cu_8O_{18\pm\delta}$ and $YBa_2Cu_3O_{7-\delta}$, Cer. Inter 44:19950–19957
58. Cakır B, Aydıner A, Karaoğlu K, Duman S, Yanmaz E (2014) Flux Pinning in YBCO Single Crystal Grown on Y_2O_3 Layer. J Supercond Nov Magn 27:1123–1129
59. Kim G, Kim C, Cheon BJ, Kim Y (2003) Variation of Pinning Mechanism in BiPbSrCaCuO Single Crystal. Phys C 391:305–308